Tropical cyclogenesis and vertical shear in a moist Boussinesq model

Qiang Deng[1], Leslie Smith[2]† and Andrew Majda[3]

[1] Department of Mathematics, University of Wisconsin, Madison, WI 53706, USA

[2] Departments of Mathematics and Engineering Physics, University of Wisconsin, Madison, WI 53706, USA

[3] Department of Mathematics and the Center for Atmosphere Ocean Science, The Courant Institute for Mathematical Sciences, New York University, NY 10012, USA

Tropical cyclogenesis is studied in the context of idealized three-dimensional Boussinesq dynamics with perhaps the simplest possible model for bulk cloud physics. With low-altitude input of water vapour on realistic length and time scales, numerical simulations capture the formation of vortical hot towers. From measurements of water vapour, vertical velocity, vertical vorticity and rain, it is demonstrated that the structure, strength and lifetime of the hot towers are similar to results from models including more detailed cloud microphysics. The effects of low-altitude vertical shear are investigated by varying the initial zonal velocity profile. In the presence of weak low-level vertical shear, the hot towers retain the low-altitude monopole cyclonic structure characteristic of the zero-shear case (starting from zero velocity). Some initial velocity profiles with small vertical shear can have the effect of increasing cyclonic predominance of individual hot towers in a statistical sense, as measured by the skewness of vertical vorticity. Convergence of horizontal winds in the atmospheric boundary layer is mimicked by increasing the frequency of the moisture forcing in a horizontal subdomain. When the moisture forcing is turned off, and again for zero shear or weak low-level shear, merger of cyclonic activity results in the formation of a larger-scale cyclonic vortex. An effect of the shear is to limit the vertical extent of the resulting emergent moist vortex. For stronger low-altitude vertical shear, the individual hot towers have a low-altitude vorticity dipole rather than a cyclonic monopole. The dipoles are not conducive to the formation of larger-scale vortices, and thus sufficiently strong low-level shear prevents the vortical-hot-tower route to cyclogenesis. The results indicate that the simplest condensation and evaporation schemes are useful for exploratory numerical simulations aimed at better understanding of competing effects such as low-level moisture and vertical shear.

Key words: stratified flows, atmospheric flows, moist convection

1. Introduction

There is now quite an extensive body of research focused on characterizing the environmental conditions necessary for the formation of tropical cyclones

† Email address for correspondence: lsmith@math.wisc.edu

(e.g. Gray 1968), as well as understanding the physical mechanisms involved (e.g. Charney & Eliassen 1964; Ooyama 1964; Emanuel 1986; Hendricks, Montgomery & Davis 2004). A recent review by Montgomery & Smith (2011) describes different paradigms that emphasize different aspects of storm intensification, and the reader may wish to consult the more extended set of references therein.

Early analyses (Charney & Eliassen 1964; Ooyama 1964) and numerical simulations (Ooyama 1969) targeted later stages of hurricane development characterized by the interaction between deep cumulus clouds and a well-defined large-scale vortex. A tropical depression leads to low-altitude convergence of warm moist air, which then allows for moist convection and latent heat release to amplify the tropical depression. Another series of papers (Emanuel 1986; Rotunno & Emanuel 1987; Emanuel 1989, 2003) highlighted the importance of the air–sea interaction, and more specifically the positive feedback between surface winds and evaporation of water from the ocean. These mechanisms focus on the amplification of an established surface vortex, rather than the genesis of the surface vortex. Once a well-defined vortex exists, it is natural to approximate the system by axisymmetric equations as in the above references.

On the other hand, cyclogenesis describes the origin of a warm-core, surface-concentrated tropical depression. During genesis, the dynamics are non-axisymmetric and probabilistic in nature (Ooyama 1982; Simpson *et al.* 1998). A pioneering paper by Riehl & Malkus (1958) recognized the importance of tall cumulonimbus clouds ('hot towers') for the energetics of the Hadley cell, and later the hot towers were also implicated in cyclogenesis (e.g. Simpson *et al.* 1998). Recent authors (Hendricks *et al.* 2004; Montgomery *et al.* 2006; Montgomery & Smith 2011; Wissmeier & Smith 2011) have elucidated the fluid dynamics and thermodynamics of rotating deep convection for the cyclogenesis problem, and have demonstrated that hot towers are the building blocks of incipient tropical depressions through merger. Following (Hendricks *et al.* 2004), we adopt the name 'vortical hot tower' (VHT) to describe tall (heights upwards of 10 km), small horizontal-scale ($\approx$10 km wide) cumulonimbus clouds with maximum values of vertical vorticity in the range 5–10×10^{-4} s^{-1} (see also Houze, Lee & Bell 2009). We here investigate whether VHTs and their merger can be captured by idealized computations of Boussinesq dynamics with a minimal moisture model. If so, then the simplified system can be used to probe aspects of cyclogenesis with the goal of deeper understanding. In particular, we use the minimal model to offer insight into the effects of vertical wind shear.

Complementary to the recent multiscale analysis (Majda, Xing & Mohammadian 2010, hereafter MXM10), our numerical study is meant to isolate fundamental physics without complicating features usually included in atmospheric cloud resolving models (CRMs) such as turbulence parametrizations, sponge layers, data-fitted background profiles and detailed cloud physics. On the one hand, the MXM10 multiscale model and the numerical model developed here should be accessible to the broader community of fluid dynamicists who would not necessarily have access to CRMs. On the other hand, these minimal models may also inform atmospheric scientists by peeling away complications in order to uncover core dynamics. In this spirit, we start with simple boundary conditions, piecewise linear background profiles and initial velocity profiles that can be expressed in terms of elementary functions. We study the response of the Boussinesq system to low-altitude, small-scale moisture bubbles, allowing for the possibility of vortical hot towers and their interaction. These low-level moisture bubbles are a surrogate for moistening due to the surface evaporation flux. Here we do not attempt to simulate the air–sea interface directly, and thus do not

address wind-induced surface heat exchange. Furthermore, since planetary rotation provides the only background vertical vorticity and our computational domain resolves horizontal scales up to 128 km, these simulations address only aspects of the genesis problem without attempting to simulate later stages of tropical storm development. In addition to the structure of a single VHT, we also study the interaction of VHTs during a simulation phase mimicking convergence of the horizontal winds in the atmospheric boundary layer. For the latter, moisture forcing seems most natural and is thus adopted for all of our current runs. As will be explained further below, the simple model used here has only two phases of water, water vapour and rain water, and does not include cloud water or ice, although cloud water can be identified directly with the excess water vapour above saturation, i.e. water loading.

It is well established that tropical storms and hurricanes develop only in an environment of low vertical shear (e.g. Gray 1968; Davis & Bosart 2004; Hendricks & Montgomery 2006; Riemer, Montgomery & Nicholls 2010). On the other hand, some case studies report differences up to 10 m s^{-1} between mean wind speeds at the top and bottom of the troposphere (e.g. Molinari, Vollaro & Corbosiero 2004). Thus it is interesting to initiate a systematic investigation into the effects of vertical wind shear on the structure and statistics of VHTs. In contrast to our simulations with varying vertical shear, Wissmeier & Smith (2011) (hereafter WS11) compared idealized simulations with varying values of planetary rotation and/or fixed background horizontal shear (providing additional vertical vorticity). They studied the evolution of a single VHT generated by a temperature anomaly, using the cloud model of Bryan & Fritsch (2002). Different cloud models and different shear profiles (horizontal versus vertical) do not allow for a direct quantitative comparison between our simulations and those of WS11. Furthermore, WS11 use background potential temperature and moisture profiles designed to match observations, whereas our background profiles are piecewise linear. Nevertheless, in a qualitative sense our results are remarkably similar to the results of WS11 incorporating more complex cloud physics, providing confidence in the simplified moisture model. One of our main contributions is to show that sufficiently strong low-altitude vertical shear leads to a vorticity dipole structure within VHTs instead of the cyclonic monopole structure associated with small vertical shear. The dipole structure in turn adversely affects the possibility of vortex merger into larger-scale moist vortices.

Related moist Boussinesq simulations have been performed in Grabowski & Clark (1991, 1993*a,b*), Grabowski & Smolarkiewicz (1996), Spyksma, Bartello & Yau (2006) and Sukhatme, Majda & Smith (2011). The evolution of a single temperature bubble in small domains (several kilometres in horizontal and vertical extent) was studied by Grabowski & Clark (1991) in two dimensions, and by Grabowski & Clark (1993*a*) in three dimensions (see also Sukhatme & Smith 2007, for aspects of the dry dynamics in two dimensions). These investigations focused on instabilities at the cloud boundary, and were extended to include the effects of environmental shear in Grabowski & Clark (1993*b*). The study by Spyksma *et al.* (2006) considered the evolution of a single moisture bubble, where periodic boundary conditions allowed for accurate calculations of liquid–water spectra at high resolutions (up to 384^3 Fourier modes). Starting from initial conditions with enough water content to saturate the domain, Sukhatme *et al.* (2011) investigated the emergence of balanced dynamics in a two-dimensional periodic domain. On the other hand, a balanced state was not attained starting from initial conditions without sufficient water substance, and then the flow remained turbulent. The work of Grabowski & Smolarkiewicz (1996) developed a semi-Lagrangian model for bulk warm-rain microphysics including cloud and rain water.

As mentioned above, a key motivational study for the current work is the multiscale model developed in MXM10 (see also Klein & Majda 2006; Majda 2007; Majda, Xing & Mohammadian 2008; Majda & Xing 2010). Using multiscale analysis, MXM10 derived a hierarchy of three coupled models for small scales and short times (10 km and 15 min), intermediate scales and short times (100 km and 15 min), and intermediate scales and longer times (100 km and 2.5 h). The coupled models are balanced, and thus simpler than the full dynamics, because they eliminate inertia–gravity waves in a spatially periodic geometry. These models elucidate the fundamental physics in each of the three space–time regimes. The authors solved the multiscale models using the same low-altitude moisture forcing adopted here with frequency 2.5 h, and showed the predominance of low-level cyclonic activity associated with VHTs, even in the presence of low-level vertical shear. We expand the study in several ways: we vary the initial velocity profile and thus the low-level shear; we vary the frequency of the moisture bubble forcing in order to investigate the detailed structure of a single VHT (forcing a bubble every 2.5 h), as well as the interaction of VHTs (forcing more frequently); after a period of forcing, we allow the flow to decay and investigate possible merger into a larger-scale moist vortex. Since our Boussinesq simulations include inertia–gravity waves, we are able to test the concept of balance for VHT generation/interaction.

The remainder of the manuscript is organized as follows. Section 2 introduces the moist Boussinesq model. In § 3 we provide details about the simulations, for example boundary conditions and the moisture forcing. Section 4 is divided into two main parts: the first part presents the benchmark case of zero initial vertical shear starting from zero initial velocity; the second half explores the dependence of the results on low-altitude vertical shear as determined by an initial zonal velocity profile. Sensitivity of the results to boundary conditions and to the latent heat factor is addressed in §§ 4.3 and 4.4, respectively. We conclude in § 5 and discuss future plans.

2. Model equations

The three-dimensional Boussinesq equations are the dynamical core of the model (Majda 2002), written in non-dimensional form as

$$\frac{D\boldsymbol{u}_h}{Dt} + \epsilon \sin(\phi)\boldsymbol{u}_h^\perp = -\boldsymbol{\nabla}_h p, \tag{2.1}$$

$$\frac{Dw}{Dt} = -\frac{\partial p}{\partial z} + \epsilon^{-1}[\theta + \varepsilon_o(q_v - q_{ve}(z)) - q_r], \tag{2.2}$$

$$\frac{D\theta}{Dt} + \epsilon^{-1}w = \epsilon^{-1}\mathscr{L}(C_d - E_r), \tag{2.3}$$

$$\boldsymbol{\nabla} \cdot \boldsymbol{u} = 0, \tag{2.4}$$

where $\boldsymbol{u} = (u, v, w)$, $\boldsymbol{u}_h = (u, v)$, $\boldsymbol{u}_h^\perp = (-v, u)$, p is a modified pressure and θ is the fluctuating part of the potential temperature. The background potential temperature is linear such that the total potential temperature is $\theta_{total} = \theta_o + Bz + \theta$. Equations (2.1)–(2.4) have been non-dimensionalized using a characteristic time $[T] = 15$ min, length scale $[L] = 10$ km, horizontal and vertical velocities $[U] \approx [L][T]^{-1} \approx 10$ m s^{-1}, and potential temperature fluctuation scale $[\Theta] = 3$ K ($B \approx 3 \times 10^{-3}$ K m^{-1}). Using buoyancy frequency $N = (Bg/\theta_o)^{1/2} = 10^{-2}$ s^{-1} and $\theta_o = 300$ K, the Froude number $Fr = ([T]N)^{-1}$ has the value $Fr \approx 0.11$. With rotation rate $\Omega \approx 7.29 \times 10^{-5}$ rad s^{-1}, the inverse Rossby number $Ro^{-1} = [T]2\Omega \sin(\phi)$ has the value $Ro^{-1} \approx 0.13 \sin(\phi)$. Therefore, after rounding, the system (2.1)–(2.4) has

been written in terms of $\epsilon = 0.1$ with $Fr^{-1} = \epsilon^{-1}$ and $Ro^{-1} = \epsilon \sin(\phi)$. In the numerical simulations, the value of $\sin(\phi)$ will be set to $\sin(\phi) = \sin(25\pi/180)$ for $\phi = 25°$ N, corresponding to dimensional Coriolis parameter $f = 2\Omega \sin(\phi) \approx 4.7 \times 10^{-5}$ s^{-1}.

The dynamical variables describing the moisture are the mixing ratios of rain water $q_r^\epsilon = \epsilon^2 q_r$ and water vapour $q_v^\epsilon = \epsilon^2 q_v$, with $q_v = q_{ve}^0(z) + \tilde{q}_v$. The initial environmental profile $q_{ve}^0(z)$ is piecewise linear, and at later times $q_{ve}(z) = q_{ve}^0 + \overline{\tilde{q}_v}$ where the overbar denotes a horizontal average. With this decomposition, it is reasonable to use zero Neumann boundary conditions at vertical boundaries for $\tilde{q}_v$. The quantity $\varepsilon_o + 1$ is the ratio of the gas constants for water vapour and dry air with $\varepsilon_o \approx 0.6$.

Focusing on (2.3) for the potential temperature, the source term involves the condensation of water vapour C_d and the evaporation of rain water E_r (Curry & Webster 1999). As in MXM10, we adopt the simple models

$$C_d = \alpha_d^{-1} (q_v - q_{vs}(z))^+, \quad E_r = \alpha_r^{-1} (q_{vs}(z) - q_v)^+ q_r \qquad (2.5)$$

where the notation $()^+$ denotes the positive part and $q_{vs}(z)$ is a specified saturation profile. Equation (2.5) imply that condensation occurs if the water vapour exceeds the saturation value, and similarly evaporation occurs if the fluid is under-saturated and if rain is present. The relaxation parameters α_d and α_r are set equal to each other with value $\alpha_d = \alpha_r = \alpha = 0.15$. Thus $\alpha^{-1} \approx \epsilon^{-1}$ is the ratio of the advective time scale $[T] \approx [L][U]^{-1}$ to the condensation/evaporation time scale $\alpha[T]$. Consistent with the linear background profile for potential temperature, we consider piecewise linear saturation profile $q_{vs}(z)$ given by

$$q_{vs}(z) = \beta - \frac{\beta}{z_o}z, \quad z \leqslant z_o, \quad q_{vs}(z) = 0, \quad z > z_o, \qquad (2.6)$$

where β is the value of the saturation water vapour mixing ratio at the surface, with typical value for the tropics $\beta = 2$ corresponding to dimensional value 20 g kg^{-1}. The pre-factor $\epsilon^{-1}\mathscr{L} = \epsilon^2 \mathscr{L}^d \theta_o ([\Theta]c_p T_o)^{-1} \approx 8$ using latent heat $\mathscr{L}^d \approx 2.5 \times 10^6$ J kg^{-1}, specific heat $c_p \approx 10^3$ J kg^{-1} K^{-1} and $\theta_o = T_o = 300$ K. Our first point of comparison is the study by MXM10 using the lower latent heat $\epsilon^{-1}\mathscr{L} = 2.4$ and correspondingly higher surface saturation $\beta = 5$. The artificially low latent heat value reduces the stiffness of the system (2.1)–(2.4), allowing for larger time steps (and thus reduced computational time) in our exploratory runs. Looking ahead to future computations aimed at quantitative comparison with CRMs, § 4.4 presents a simulation with realistic values $\epsilon^{-1}\mathscr{L} = 8$ and $\beta = 2$. Finally, in (2.6), the value of z_o is set to $z_o = 1.2$ (corresponding to 12 km).

Consistent evolution equations for $\tilde{q}_v$ and q_r are given by

$$\frac{D\tilde{q}_v}{Dt} + \frac{\partial q_{ve}^0(z)}{\partial z}w = -(C_d - E_r), \qquad (2.7)$$

$$\frac{Dq_r}{Dt} - V_T\frac{\partial q_r}{\partial z} = C_d - E_r, \qquad (2.8)$$

where the (constant) rain velocity will be set to $V_T = 0.5$ corresponding to the dimensional value 5 m s^{-1}. We will assume an initial environmental profile that is slightly under-saturated,

$$q_{ve}^0(z) = (q_{vs}(z) - \delta)^+, \qquad (2.9)$$

and the value of δ will be set to $\delta = \beta/32$. This is consistent with order-of-magnitude environmental preconditioning for cyclogenesis (Gray 1968; Montgomery & Smith 2011). Note that the simplified system (2.1)–(2.8) does not include explicit equations for cloud water, such that condensation leads directly to rain. However, when the cloud vapour q_v exceeds saturation in the simplified dynamics, this saturation excess can be interpreted as cloud water. For a discussion of the conservation principles of moist systems, see Frierson, Pauluis & Majda (2004).

As mentioned in §1, MXM10 performed a multiscale analysis of the anelastic analogue of (2.1)–(2.4), yielding three coupled models for the fast microscales ($[T] = 15$ min and $[L] = 10$ km), the fast mesoscales ($[T] = 15$ min, $[L_m] = \epsilon^{-1}[L] = 100$ km) and the slow mesoscales ($[T_m] = \epsilon^{-1}[T] = 2.5$ h, $[L_m] = 100$ km). The weak temperature gradient (WTG) approximation $w = \mathscr{L}(C_d - E_r)$ replacing (2.3) is a key element of the fast microscale model, leading to the elimination of inertia–gravity waves, whereas the fast mesoscale model incorporates linear hydrostatic gravity waves. With a low-altitude moisture forcing in a periodic geometry where the effects of the mesoscale hydrostatic gravity waves vanish, MXM10 demonstrated that the coupled multiscale models capture the formation of VHTs and the predominance of low-altitude cyclonic activity on long time scales of roughly four days. The present numerical simulations of (2.1)–(2.9) indicate that the presence of inertia–gravity waves does not qualitatively change the physical mechanisms captured by the multiscale analysis leading to generation of VHTs.

3. Simulation details

Equations (2.1)–(2.9) are solved in a three-dimensional domain with periodic boundary conditions in both horizontal directions and a combination of Dirichlet/Neumann boundary conditions on the top and bottom. The numerical solution uses a pseudo-spectral decomposition in the horizontal directions, and a second-order centred difference scheme on a staggered grid in the vertical direction. The numerical domain is $12.8 \times 12.8 \times 1.5$ corresponding to 128 km $\times$ 128 km $\times$ 15 km. We use 128 Fourier modes in each horizontal direction and 100 grid points in the vertical direction resulting in horizontal resolution $\Delta x = \Delta y = 0.1$ (1 km) and vertical resolution $\Delta z = 0.015$ (0.15 km). Time-stepping proceeds according to the third-order Runge–Kutta scheme. The time step is set to 0.01 corresponding to 0.15 min in physical units, which is below the minimum of the Courant–Friedrichs–Lewy (CFL) condition and a condition to sample the highest-frequency inertia–gravity wave with at least ten steps per full period. According to the CFL and wave resolution conditions, the time step is lowered according for higher-resolution runs with 512 Fourier modes in each horizontal direction §4.2.2.

The bottom of the domain at $z = 0$ is meant to crudely represent the top of the atmospheric boundary layer, while the top of the domain at $z = H = 1.5$ (15 km) roughly mimics the tropopause. For no flow through the boundary layer/tropopause, we set

$$w|_{z=0,H} = 0. \tag{3.1}$$

For most of the runs presented here, the horizontal velocity has zero Neumann boundary condition at the tropopause and zero Dirichlet boundary condition at the boundary layer such that

$$\left.\frac{\partial \boldsymbol{u}_h}{\partial z}\right|_{z=H} = 0, \quad \boldsymbol{u}_h|_{z=0} = 0. \tag{3.2}$$
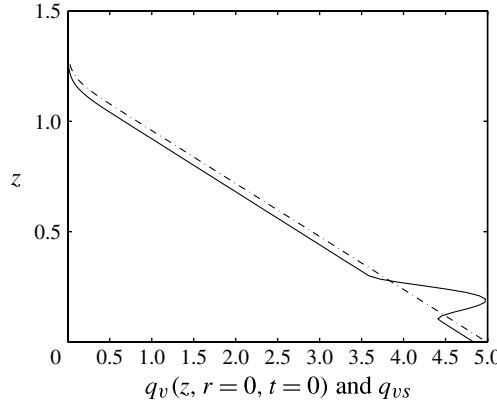
FIGURE 1. Initial water vapour profile $q_v(z, r = 0, t = 0)$ (solid line) and saturation profile $q_{vs}(z)$ (dashed line).

However, we also present the results of selected runs with Neumann condition at the bottom of the domain $(\partial \boldsymbol{u}_h / \partial z)|_{z=0} = 0$ (see § 4.3). For all other variables $f = \theta, \tilde{q}_v, q_r$ we use zero Neumann boundary conditions on the top and bottom, such that

$$\left. \frac{\partial f}{\partial z} \right|_{z=0,H} = 0. \tag{3.3}$$

For dissipation in (2.1)–(2.3), (2.7)–(2.8), we add a horizontal hyperviscosity term $-\mu_1 \nabla_h^4 f$ ($f = \boldsymbol{u}_h, w, \theta, \tilde{q}_v, q_r$) to the right-hand side, where

$$\mu_1 = \frac{D_4}{K_{max}^4 \Delta t}, \quad K_{max} = ((\pi/\Delta x)^2 + (\pi/\Delta y)^2)^{1/2}, \quad \nabla_h^4 = \left(\frac{\partial^2}{\partial x^2} + \frac{\partial^2}{\partial y^2} \right)^2, \tag{3.4}$$

with value $D_4 = 0.1$. In the vertical direction, since we are using a finite difference scheme, we use the normal viscosity $\mu_2 \partial^2 f / \partial z^2$, where

$$\mu_2 = D_2 \frac{(\Delta z)^2}{\Delta t}, \tag{3.5}$$

with $D_2 = 0.005$.

In all simulations, the initial water vapour anomaly is given by

$$\tilde{q}_v(x, y, z)|_{t=0}$$
$$= \begin{cases} (0.8 + \delta) [10(z - 0.1)]^2 [10(z - 0.3)]^2 \cos(\pi r) & r \leqslant 0.5, \, 0.1 \leqslant z \leqslant 0.3, \\ 0 & r > 0.5, \end{cases} \tag{3.6}$$

where $r \equiv \sqrt{(x - x_0)^2 + (y - y_0)^2}$, and (x_0, y_0) is a random horizontal location and represents the centre of the moisture bubble. Thus the system is super-saturated for low altitudes $0.1 < z < 0.3$ (1–3 km) and under-saturated at all other altitudes. Figure 1 shows the initial water vapour profile $q_v = \tilde{q}_v + q_{ve}^0$ at $r = 0$ along with the saturation profile. The radius of the low-level moisture bubble is 5 km and its vertical extent is 2 km. The same shape water vapour bubble is added to the system every 2.5 h (10 time units) at a random horizontal location (x_0, y_0) for approximately 4 days (400 time units). During this period, we investigate the structure of the VHTs

and sensitivity to low-altitude vertical shear. After 4 days, the bubble is added more frequently over a period of ∼2.6 days (250 time units). Furthermore, the centre of the bubble is confined to a horizontal subdomain (4 km × 4 km). More frequent moisture forcing in a horizontal subdomain is a surrogate for convergence of the horizontal wind field in the boundary layer. The moisture forcing is turned off at 6.6 days, after which time we look for the formation of a larger-scale vortices.

4. Simulation results

4.1. *Benchmark simulation with zero initial velocity*

In this section we present the results from a simulation with zero initial velocity and low-altitude moisture forcing as described above. This run (denoted Run 0) is closest to WS11 cases 6 and 7 with no horizontal shear and Coriolis parameter $f \approx 4.7 \times 10^{-5}$ s^{-1}. WS11 cases 6 and 7 differ by the amplitude of the low-altitude temperature bubble used to initiate a VHT. We note that WS11 follow the evolution of a VHT after the input of a low-altitude temperature anomaly, rather than a moisture anomaly. Many of the results in WS11 pertain to other cases with higher values of the background rotation and/or fixed uniform horizontal shear. Other differences render a quantitative comparison impossible, e.g. the cloud model of Bryan & Fritsch (2002), the background potential temperature and moisture profiles, and a sponge layer at the top of the domain. However, all of our results are qualitatively similar to the plots presented in WS11. In our greyscale plots, white denotes maximum contour levels, e.g. of vorticity, vertical velocity and rain water. There should be no confusion between white local maxima and white background, since local maxima occur inside the VHT structures, but we alert the reader to this issue.

4.1.1. *The structure of the vortical hot towers*

Figure 2 shows a single contour level of the water vapour anomaly $\tilde{q}_v$ at times 0, 15, 30 and 45 min after the injection of a moisture bubble at the end of the 4-day period with forcing frequency every 2.5 days. The contour level corresponds to 1.2 g kg^{-1}, which is roughly 15 % of the maximum value reached 15 min after the bubble injection. The relatively low contour level (compared to the maximum) allows one to visualize the exterior structure of the VHT; the highest values of water vapour are achieved inside the tower. The moisture rises well above 10 km, and the tower is intact for at least 45 min. Figure 3 shows companion vertical vorticity contours up to altitude 5 km, and at times 30 and 45 min after the bubble injection. The two contour levels are $\pm 4 \times 10^{-4}$ s^{-1}, and one can see a predominance of positive vertical vorticity below 3 km in the VHT. To better visualize the structure of the vorticity, it is helpful to view contours in a horizontal plane at fixed altitude. Such horizontal slices are presented in figure 4 at altitude 1.5 km, and at the same times as in figure 3. Only a portion of the horizontal plane is included in order to zoom in on the vorticity monopole structure of the VHT. Since one vorticity unit is 10^{-3} s^{-1}, there is a maximum vertical vorticity of $\sim 8 \times 10^{-4}$ s^{-1} at 30 min after the bubble injection. The diameter of the VHT is roughly 5 km, matching the horizontal extent of each moisture bubble. The study by Houze *et al.* (2009) reported observations of VHTs in pre-hurricane Ophelia with maximum values of vertical vorticity in the range 5–10×10^{-4} s^{-1}. Their measurements reflected VHT dimensions of ~ 10 km wide and 17 km high.

Figures 5 and 6 present, respectively, contours of the maximum vertical velocity w and contours of the maximum rain water q_r, as functions of time (abscissa) and
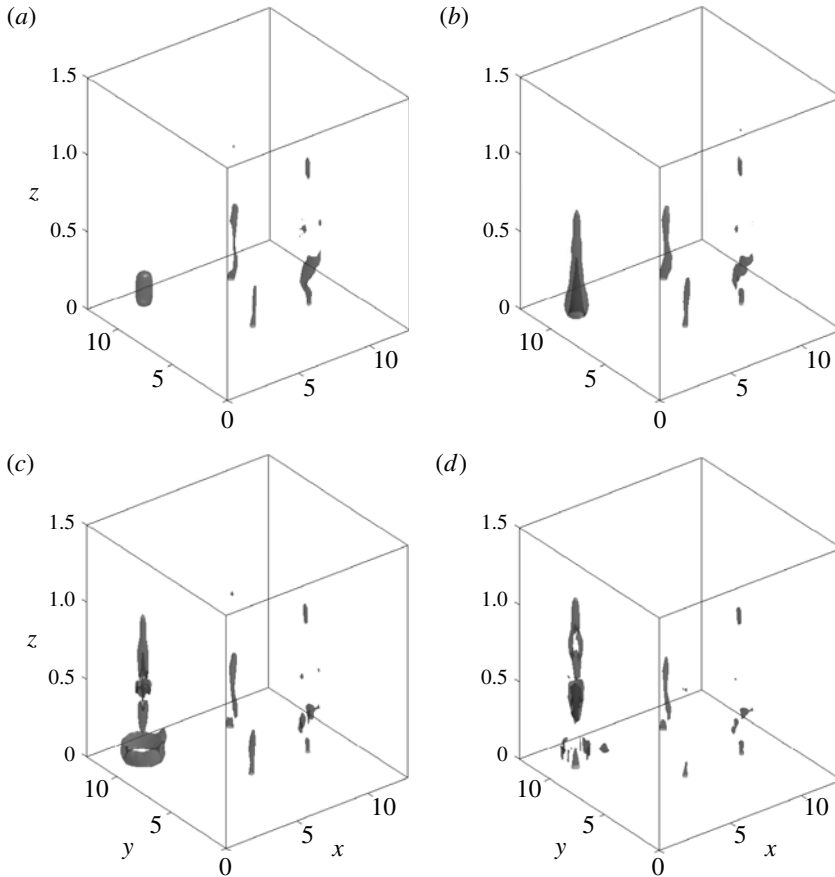
FIGURE 2. Moisture anomaly contours for Run 0 (the contour level is 1.2 g kg^{-1}). The times are (*a*) 0 min, (*b*) 15 min, (*c*) 30 min and (*d*) 45 min after a bubble injection at approximately 4 days. One unit of distance = 10 km.

altitude (ordinate). Time is rescaled so that the beginning time $t = 0$ is the time of a moisture bubble injection. Since one time unit is 15 min, both plots indicate that the lifetime of a VHT is approximately 1 h. During this representative VHT event, the maximum of vertical velocity of approximately 14 m s^{-1} occurs at $\sim$5 km high and roughly 10 min after the bubble injection. Figure 5 shows that the relative maximum moves to higher altitudes as time progresses, up to $\sim$30 min. Similarly, the maximum of rain water occurs at $\sim$10 min after the bubble injection, and reaches a value 16 g kg^{-1} at an altitude close to 6 km high (figure 6). After 10–15 min, it rains more at altitudes lower than 5 km. However, smaller values of rain water can be seen as high as 10 km approximately 45 min into the VHT lifetime.

4.1.2. *Decay into a larger-scale moist vortex*

The VHT structure observed in the plots of § 4.1.1 follows each bubble injection every 2.5 h over a period of 4 days. The 4-day time period was chosen to obtain good time-averaged statistics for the low-altitude vertical vorticity associated with the VHTs (see table 1). After the 4-day period, in order to mimic convergence of the horizontal winds in the atmospheric boundary layer, we increase the frequency of
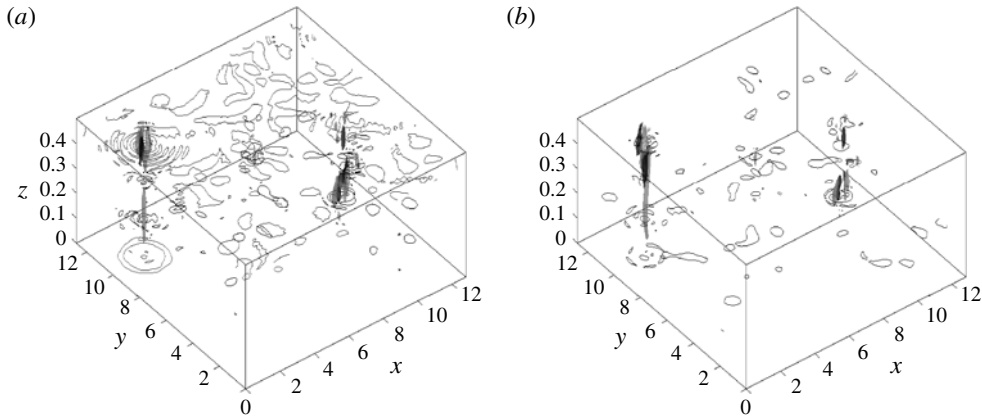
FIGURE 3. Three-dimensional vertical vorticity contours for Run 0 (light grey $= 4 \times 10^{-4}$ s^{-1}, dark grey $= -4 \times 10^{-4}$ s^{-1}). The times are (*a*) 30 min and (*b*) 45 min after a bubble injection at approximately 4 days (the same injection time as in figure 2). One unit of distance $=$ 10 km. The curves are two-dimensional contour lines at altitudes $z = 1.5, 3.0$ and 4.5 km. See figure 4 for contour levels between -2×10^{-4} and 8×10^{-4} s^{-1} at altitude $z = 1.5$ km.
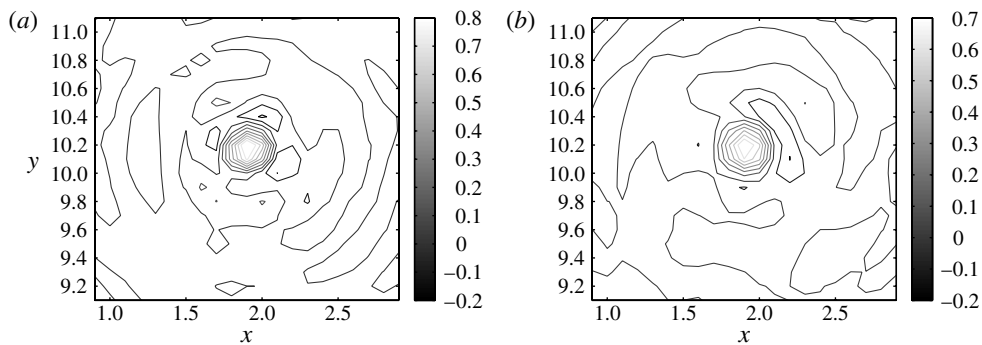
FIGURE 4. Two-dimensional vertical vorticity contours at $z = 1.5$ km for Run 0. The times are (*a*) 30 min and (*b*) 45 min after a bubble injection at approximately 4 days (the same injection time as in figures 2 and 3). One vorticity unit $= 10^{-3}$ s^{-1}; one unit of distance $=$ 10 km.

t (0, 4 days)	Zero (Run 0)	Non-skew (Run 1)	Bottom-skew (Run 2)	Top-skew (Run 3)
$z = 1.5$ km	0.26	0.28	0.11	0.42
$z = 3.0$ km	0.06	0.02	0.05	0.13
$z = 4.5$ km	-0.02	0.03	-0.02	-0.01

TABLE 1. The time-averaged values of vertical vorticity skewness given by (4.5) for Runs 0–3 at altitudes $z = 0.15, 0.30, 0.45$ corresponding to 1.5, 3.0, 4.5 km.

the bubble forcing to once every 7.5 min, and confine the random position of each bubble to lie within a horizontal subdomain of size 4 km $\times$ 4 km. The more frequent
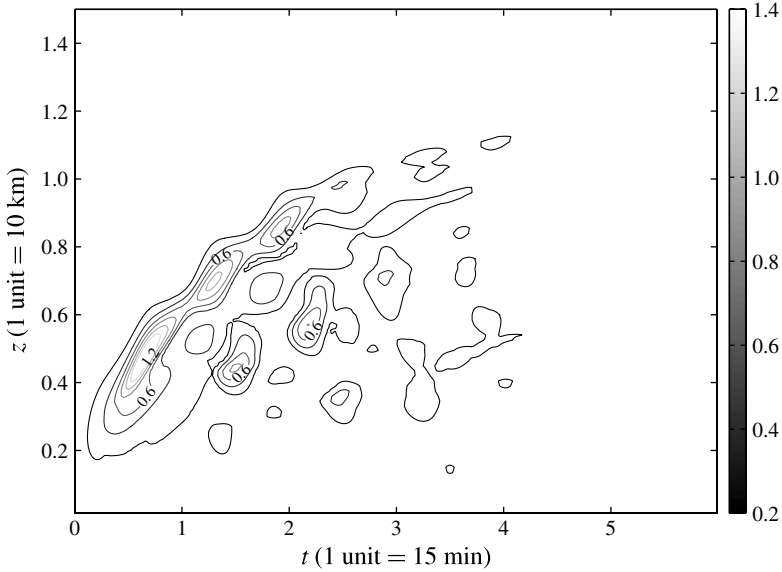
FIGURE 5. Maximum vertical velocity versus time (abscissa) and altitude (ordinate) for Run 0: lifetime $\approx$1 h; one velocity unit = 10 m s^{-1}. Contours are spaced by 0.2 velocity units.
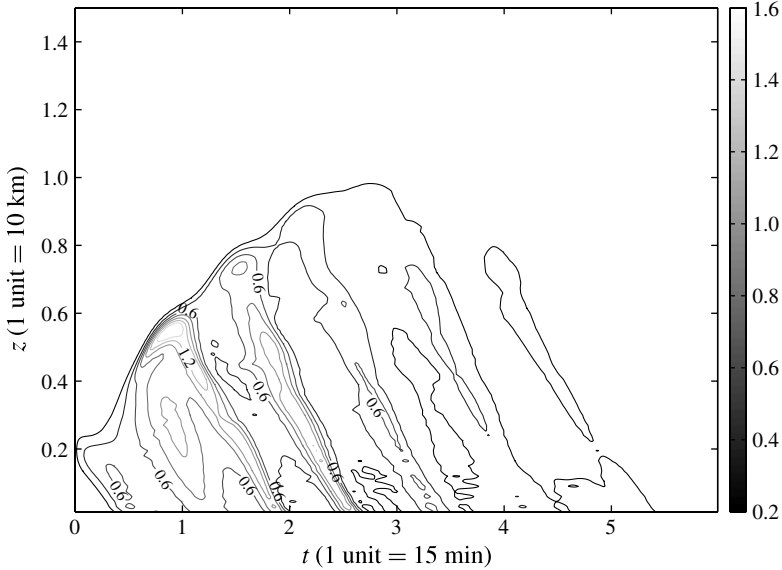

FIGURE 6. Maximum liquid water versus time (abscissa) and altitude (ordinate) for Run 0: lifetime $\approx$1 h; one unit of rain water = 10 g kg^{-1}. Contours are spaced by 0.2 units of rain water.

forcing is applied for 250 time units corresponding to 2.6 days. After a total time of 6.6 days, the moisture forcing is turned off and the flow is allowed to evolve
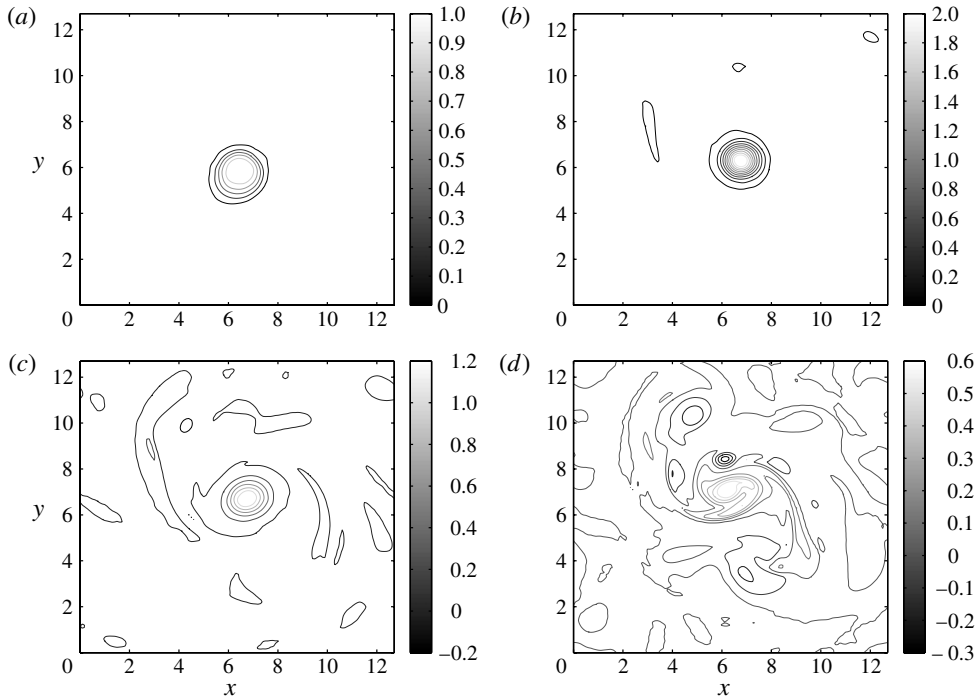
FIGURE 7. Two-dimensional vertical vorticity contours for Run 0 (zero initial velocity) at altitudes (*a*) 1.5 km, (*b*) 3.0 km, (*c*) 4.5 km and (*d*) 6.0 km. The time is 9 h into the decay period. One unit of vorticity $= 10^{-3} \text{s}^{-1}$.

freely. The low-level positive vorticity quickly merges into a single larger-scale vortex, which is well developed roughly 2 h after the forcing is ceased. Figure 7 shows the vortex 9 h into the decay period, at height levels 1.5, 3.0, 4.5 and 6.0 km. One can see a vortical column aligned with the *z*-axis up to 4.5 km, with some deterioration of the vortex at 6.0 km high. At that time, the vorticity amplitude of the vortex is $\sim 10^{-3}$ s^{-1} at 1.5 km and roughly twice as strong at height 3.0 km. The diameter of the vortex is roughly 20 km, which is about twice as large as the diameter of the VHTs. For Run 0 with zero initial velocity, results similar to figure 7 (not shown) were obtained with bubble forcing frequency of 15 min in a horizontal subdomain of 16 km × 16 km. However, for Run 3 with low-altitude shear (see below), stronger 'convergence' (i.e. smaller domain, higher frequency) was necessary in the period preceding decay in order to obtain a well-defined, larger-scale cyclone. Therefore we present only the results from the 'strong convergence' experiment throughout (7.5 min frequency, 4 km × 4 km subdomain).

4.2. *Low-altitude vertical shear*

We now compare the benchmark Run 0 (zero initial velocity) to Runs 1–3 with varying vertical shear as determined by an initial zonal velocity profile $\boldsymbol{u} = u(t = 0, z)\hat{\boldsymbol{x}}$. Figure 8 shows initial and later-time mean horizontal velocity profiles $\overline{U}(z) = (\bar{u}^2 + \bar{v}^2)^{1/2}(z)$ for these runs, where the bar denotes a horizontal average. Run 1 starts with zonal velocity profile that is symmetric about $z = 7.5$ km, and has
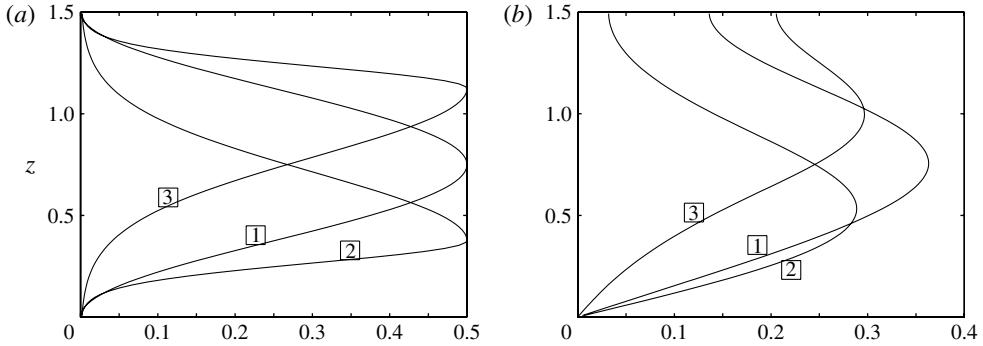
FIGURE 8. (*a*) Initial zonal velocity with $u(t = 0, z)$. (*b*) Horizontal mean velocity $\overline{U}(z) = (\bar{u}^2 + \bar{v}^2)^{1/2}(z)$ at $t = 400$ units (approximately 4 days). One velocity unit $= 10$ m s^{-1}; one height unit $= 10$ km.

maximum value 5 m s^{-1}:

$$\text{Run 1:} \quad u(t = 0, z) = 0.25\bigl(1 - \cos(2\pi z/L_z)\bigr), \tag{4.1}$$

where $L_z = 1.5$ in the vertical height of the domain. The initial profiles for Runs 2 and 3 shift the maximum velocity down/up. They are constructed using the exponential function as follows:

$$\text{Run 2:} \quad u(t = 0, z) = 0.5 \exp\bigl(-96\,(z - L_z/4)^2\,/L_z^2\bigr), \quad z \leqslant L_z/4,$$

$$u(t = 0, z) = 0.5 \exp\bigl(-10\,(z - L_z/4)^2\,/L_z^2\bigr), \quad z > L_z/4, \tag{4.2}$$

$$\text{Run 3:} \quad u(t = 0, z) = 0.5 \exp\bigl(-10\,(z - 3L_z/4)^2\,/L_z^2\bigr), \quad z \leqslant 3L_z/4,$$

$$u(t = 0, z) = 0.5 \exp\bigl(-96\,(z - 3L_z/4)^2\,/L_z^2\bigr), \quad z > 3L_z/4, \tag{4.3}$$

and also named 'non-skew' (Run 1), 'bottom-skew' (Run 2) and 'top-skew' (Run 3) in reference to the position of the maximum. The mean velocity profiles evolve according to viscous effects and nonlinear momentum transport:

$$\frac{1}{2}\frac{\partial(\bar{u}^2 + \bar{v}^2)}{\partial t} = -\left(\bar{u}\frac{\partial\overline{uw}}{\partial z} + \bar{v}\frac{\partial\overline{vw}}{\partial z}\right) + \nu_2\left(\bar{u}\frac{\partial^2\bar{u}}{\partial z^2} + \bar{v}\frac{\partial^2\bar{v}}{\partial z^2}\right). \tag{4.4}$$

The viscous terms contribute the most change to the mean profiles in figure 8, even though the momentum transport terms are critical to the local structure of the VHTs. For example, without the nonlinear transport terms, the cloud tops are limited to below $z = 0.4$ (4 km) with maximum vertical velocities about 0.7 (7 m s^{-1}). Throughout the 4-day interval, Run 3 (Run 2) has the smallest (largest) low-level vertical shear below $z \approx 0.3$. Notice that by $t = 400$, the low-level shear profiles of Runs 1 and 2 are quite similar, and larger than for Run 3.

   In order to gather statistics on the low-altitude vorticity of the VHTs, we ran the simulations for Runs 0–3 for 400 time units (approximately 4 days) with the low-frequency bubble forcing every 2.5 h. The centre of each bubble was chosen as a random position in the horizontal domain. During this period, the VHTs evolve independently of each other, since the lifetime of a VHT is approximately 1 h. At a
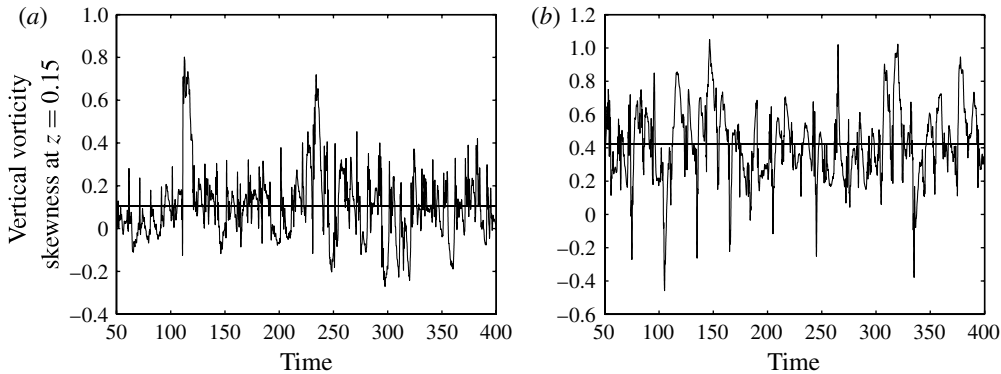
FIGURE 9. The skewness of vertical vorticity $S(t, z = 0.15)$ given by (4.5) for (*a*) bottom-skew Run 2 and (*b*) top-skew Run 3. The line is the time-averaged value (see also table 1). (*a*) Average value $= 0.11$; (*b*) average value $= 0.42$.

fixed altitude, we then measured the skewness S of the vertical vorticity as given by

$$S(t, z) = \frac{N}{L_x} \frac{\displaystyle\sum_{ix,iy=1}^{N} \left(\omega_{ix,iy} - \bar{\omega} \right)^3}{\left(\displaystyle\sum_{ix,iy=1}^{N} \left(\omega_{ix,iy} - \bar{\omega} \right)^2 \right)^{3/2}}, \tag{4.5}$$

where $N = 128$ is the number of grid points in each horizontal direction, $L_x = 12.8$ (128 km) is the length of the domain in the x- and y-directions, and $\bar{\omega}$ is the horizontal mean value of the vertical vorticity at the given z-level and time t. The skewness S is a statistical measure of the sense of vorticity for individual VHTs. Figure 9 shows $S(t, z = 0.15)$ for the bottom-skew Run 2 and top-skew Run 3 as a function of time and fixed altitude $z = 0.15$. Time starts at 50 time units (12.5 h) to avoid start-up issues during the first time steps (some fields are initialized to zero). The solid line is the time-averaged value (see also table 1 for the time-averaged values of Runs 0–3 at altitudes $z = 0.15, 0.30, 0.45$). Both Runs 2 and 3 have positive time-averaged value of $S(t, z = 0.15)$, and notice the large fluctuations in amplitude indicating significant variation in the structure of individual VHTs. Statistically, at the lowest levels $z = 0.15$ and $z = 0.30$, the top-skew Run 3 with small low-altitude vertical shear shows the most tendency for cyclonic activity. The benchmark Run 0 and non-skew Run 1 have similar skewness values at $z = 0.15$ (table 1). However, we will show in § 4.2.3 that only Runs 0 and 3 produce a well-defined, vertically coherent, larger-scale vortex during the decay period following 'convergence'. Thus the value of the vertical vorticity skewness characterizing individual VHTs is, by itself, not enough to predict the outcome of nonlinear interactions among VHTs (compare Runs 0 and 1).

4.2.1. *The structure of the vortical hot towers*

Having investigated the statistical tendency for VHTs to be predominantly cyclonic at low altitude (table 1), we now further examine structural aspects of representative VHTs for Runs 1–3 and compare to Run 0. Figure 10 shows the moisture anomaly $\tilde{q}_v$ for Runs 2 and 3, at time 30 min after a bubble injection. Both panels appear quite similar to t figure 2(*c*). Thus it is clear that hot towers are generated by the moisture
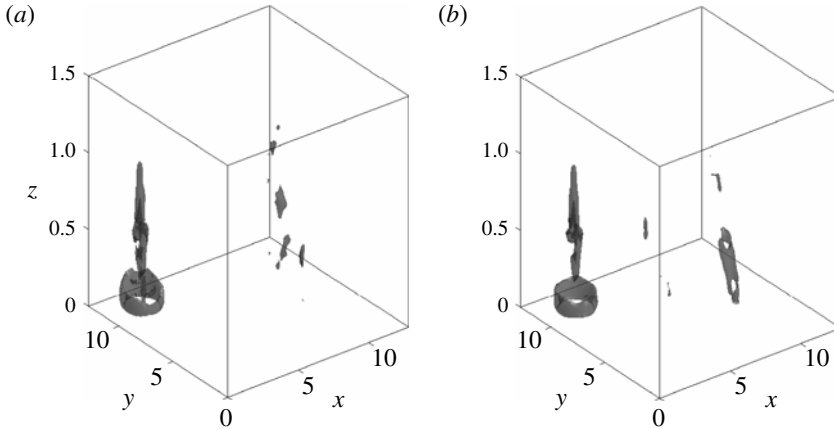
FIGURE 10. Moisture anomaly contours for (*a*) bottom-skew Run 2 and (*b*) top-skew Run 3 at 30 min after a bubble injection at approximately 4 days (the same time as for figures 2–4). The contour level 1.2 g kg^{-1} is the same as in figure 2. One unit of distance $= 10$ km.
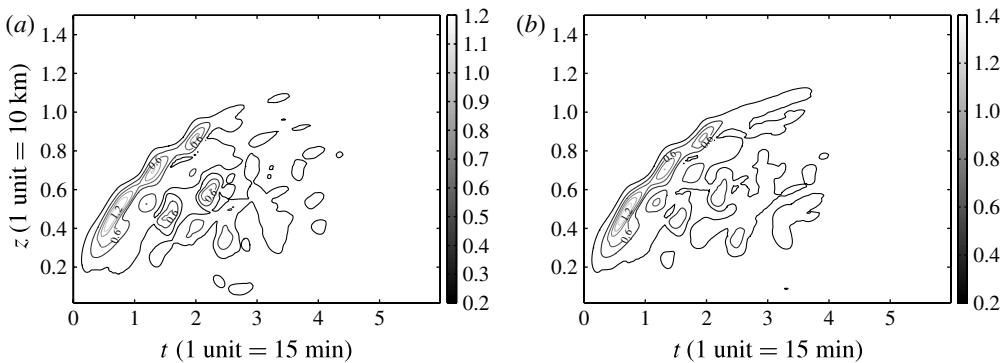

FIGURE 11. Maximum vertical velocity versus time (abscissa) and altitude (ordinate) for (*a*) bottom-skew Run 2 and (*b*) top-skew Run 3: lifetime ≈ 1 h; one velocity unit $= 10$ m s^{-1}. Contours are spaced by 0.2 velocity units.

forcing in all Runs 0–3. Similarly the maximum vertical velocity and maximum rain signatures (figures 11 and 12) are close to those for Run 0 (figures 5 and 6), though the maximum vertical velocity is smaller for the bottom-skew Run 2 with value 12 m s^{-1} (compared to 14 m s^{-1} for Runs 0 and 3).

However, the low-level ($z = 1.5$) two-dimensional vertical vorticity contours are noticeably different for each run (figure 13). The dipole structure of Run 2 and the monopole cyclonic structure of Run 3 are quite clear in the low-altitude two-dimensional contour plots. One can anticipate that vortex merger of the VHTs in Run 3 may lead to a larger-scale cyclonic vortex, while no such possibility exists for Run 2. Though figure 13 is indicative of structural differences between runs, it is important to keep in mind the variation in magnitude and shape for individual VHT events.

As mentioned above, the multiscale model of MXM10 filters inertia–gravity waves using the WTG approximation, whereas our computations resolve those waves. By
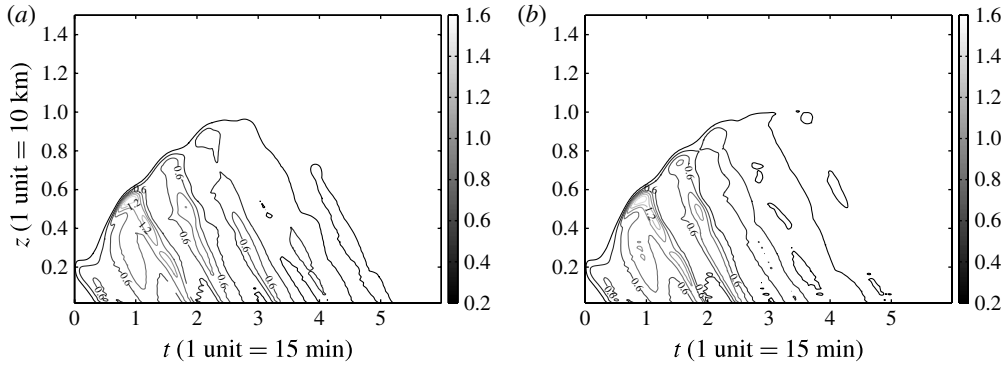
FIGURE 12. Maximum liquid water versus time (abscissa) and altitude (ordinate) for (*a*) bottom-skew Run 2 and (*b*) top-skew Run 3: lifetime ≈ 1 h; one unit of rain water $= 10$ g kg^{-1}. Contours are spaced by 0.2 units of rain water.
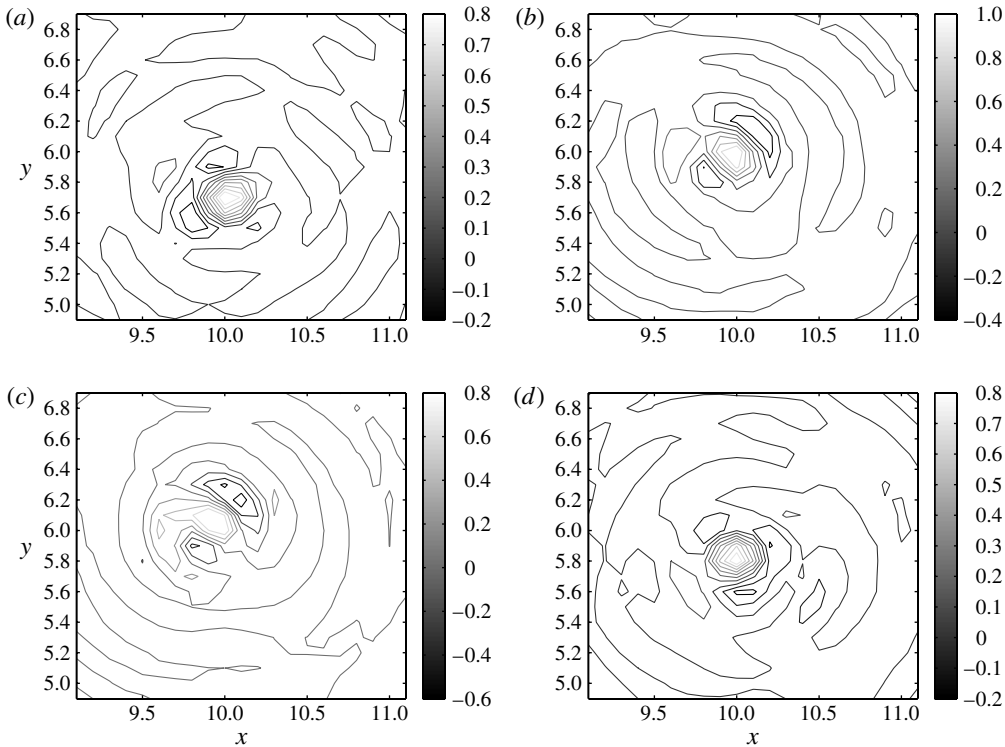

FIGURE 13. Two-dimensional vertical vorticity contours at $z = 1.5$ km for (*a*) Run 0, (*b*) non-skew Run 1, (*c*) bottom-skew Run 2 and (*d*) top-skew Run 3. The time is 30 min after a bubble injection. One vorticity unit $= 10^{-3}$ s^{-1}; one unit of distance $= 10$ km.

viewing the difference between the vertical velocity and the source terms in (2.3), one clearly sees that inertia–gravity waves radiate away from the VHTs (figure 14). Both plots for Runs 2 and 3 show the difference at altitude 1.5 km and 2.25 h after
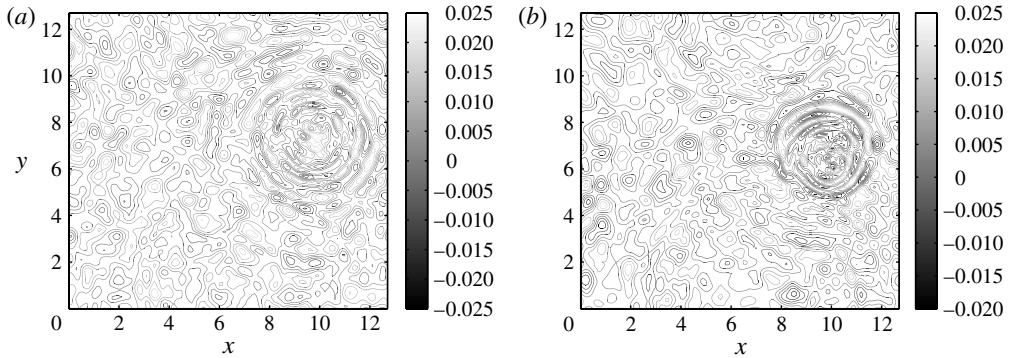
FIGURE 14. Difference between vertical velocity w and heat source $L(C_d - E_r)$ 2.25 h after the injection of a moisture bubble. The signature of the inertia–gravity waves is evident. *a*: Run 2 (bottom-skew); *b*: Run 3 (top-skew).

the injection of a moisture bubble. It remains to understand more precisely how the inertia–gravity waves may change the eventual merger of low-altitude cyclonic activity into a larger-scale, vertically coherent moist vortex, in cases such as Runs 0 and 3 when the latter occurs. Studies of inertia–gravity waves in dry dynamics indicate that their nonlinear interactions are crucial for a complete understanding of coherent structure formation (e.g. Smith & Lee 2005; Remmel & Smith 2009).

4.2.2. *Monopole versus dipole vorticity*

Section 4.2.1 demonstrated that sufficiently strong low-altitude vertical shear inhibits cyclogenesis by changing the vertical vorticity structure of VHTs from a cyclonic monopole (low shear) to a dipole (sufficiently strong shear). When a moisture bubble anomaly is introduced, latent heat release from condensation leads to upward motion of locally warmer air. Horizontal divergence from the warm core in the presence of (only) planetary vorticity creates a VHT with a positive vertical vorticity anomaly (figure 16). In the presence of a horizontal velocity, the rising warm air is also dragged downstream. If the vertical shear associated with the velocity profile is strong enough, a low-speed streak will develop, flanked by oppositely signed vertical vorticity in a horizontal slice through the VHT (figure 17).

One may gain insight into the vorticity structure of the hot towers by imposing an idealized, background velocity profile. Assuming WTG in an infinite domain, Majda *et al.* (2008) showed that there are exact linear solutions for the vertical and horizontal velocities, with parameters that determine the underlying cloud structure (e.g. stratiform type with rising air above descending air or congestus type with rising air below descending air). Then, using the vorticity equation, Majda *et al.* (2008) studied the emergence of cyclones or anticyclones depending on the parameters. Here we adopt a similar approach and linearize the equation for the vertical vorticity about prescribed vertical and horizontal velocity profiles. The background velocity profiles are chosen to approximate the simulation results at low altitudes $0.1 \leqslant z \leqslant 0.3$ and short times after a moisture bubble has been introduced at $x = x_o$, $y = y_o$ with horizontal radius $r_o \approx 0.5$. Thus we consider a linear background zonal profile $U(z) = Sz$, $S > 0$ and zero background meridional flow $V = 0$. The vertical velocity is approximated by

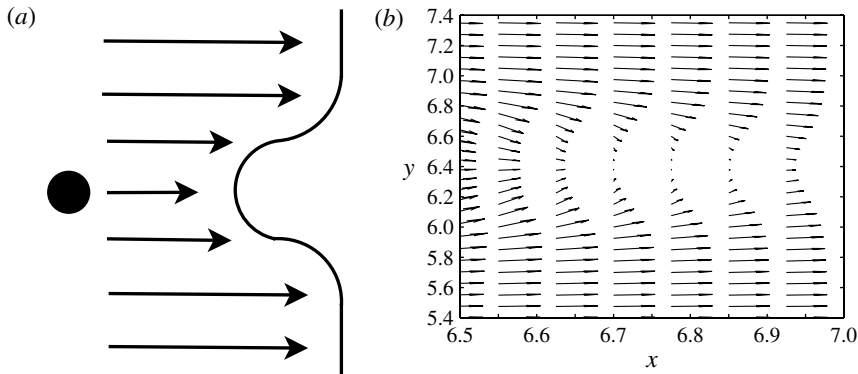$$w = Rz \exp(-[(x - x_o)^2 + (y - y_o)^2]/r_o^2) \tag{4.6}$$

FIGURE 15. (*a*) A sketch illustrating how a blob of low-speed fluid originating from lower altitude leads to a low-speed streak. (*b*) Horizontal velocity vectors at $z = 0.15$ for Run 2 at higher resolution $512 \times 512 \times 100$. The time is approximately 7 min after the first bubble injection, and the (negative) local minimum has been subtracted from the horizontal velocity for comparison with the sketch.
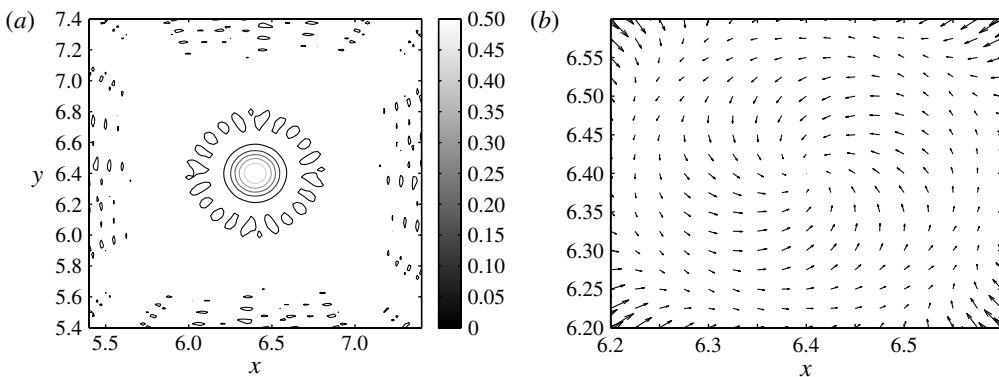

FIGURE 16. A horizontal slice at $z = 0.15$ for Run 0 at higher resolution $512 \times 512 \times 100$: (*a*) contours of vertical vorticity; (*b*) horizontal velocity vectors. The time is approximately 15 min after the first bubble injection.

consistent with rising warmer fluid ($R > 0$) localized near the bubble centre (x_o, y_o), and satisfying the bottom boundary condition $w(z = 0) = 0$ (or implying a stratiform-type cloud in an infinite z-domain). With $u = U(z) + u'$, $v = v'$, a standard linearization of the horizontal momentum equation (2.1), and assuming $\partial u'/\partial z, \partial v'/\partial z \ll S$, leads to the equation for the vertical vorticity ω_z:

$$\frac{\partial \omega_z}{\partial t} + U \frac{\partial \omega_z}{\partial x} \approx f \frac{\partial w}{\partial z} - S \frac{\partial w}{\partial y}$$

$$= R \left(f - 2 \frac{(y - y_o)}{r_o^2} S \right) \exp(-[(x - x_o)^2 + (y - y_o)^2]/r_o^2). \quad (4.7)$$

There are two source terms on the right-hand side of (4.7) originating from the planetary vorticity f and the vertical shear S, both involving derivatives of the vertical
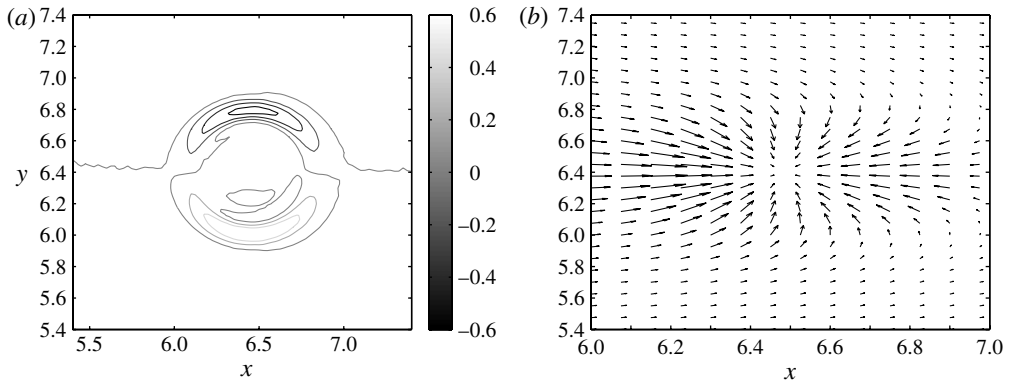
FIGURE 17. A horizontal slice at $z = 0.15$ for Run 2 at higher resolution $512 \times 512 \times 100$: (*a*) contours of vertical vorticity; (*b*) horizontal velocity vectors. The time is approximately 7 min after the first bubble injection.

velocity w and proportional to $R > 0$. In the absence of shear S, it is clear that positive vertical vorticity is generated inside the VHT core for $|x - x_o| < r_o$, $|y - y_o| < r_o$ (figure 16). When S is large enough, the second source term dominates and changes sign: it is positive for $y < y_o$ and negative when $y > y_o$, thus creating a dipole in vertical vorticity (figure 17). Note that u' and v' exchange momentum through the Coriolis terms, such that the horizontal mean is not necessarily in the zonal direction at bubble injection times after $t = 0$. Then the toy model illustrates the short time dynamics after an appropriate rotation of the horizontal axes.

In the simulations as time progresses during the lifetime of a VHT, we observe alternating cyclonic and anticyclonic vertical vorticity in the VHT core at low altitudes: in the weak shear case, the sign of the monopole changes; in the strong shear case, new dipoles are formed with alternating sign of vorticity in each lobe. The alternating vorticity happens because generation of inertia–gravity waves leads to oscillations in the vertical velocity such that w changes sign at the centre (x_o, y_o) of the VHT (see figure 14 for evidence of the inertia–gravity waves). In the context of the toy model (4.6)–(4.7), negative w with $R < 0$ leads to an anticyclone (weak shear case), or a dipole with positive vertical vorticity for $y > y_o$ and negative vertical vorticity for $y < y_o$ (strong shear case). However, each subsequent bubble injection always leads to the sense of vorticity implied by (4.7) with $R > 0$ (figures 16 and 17). Frequent and confined bubble forcing in low-shear runs (§§ 4.1.2 and 4.2.3) deposits cyclonic VHTs close together such that merger into a larger-scale, moist cyclonic vortex can occur.

4.2.3. *Decay into a larger-scale moist vortex*

The biggest difference between the bottom-skew Run 2 with larger low-altitude shear and the top-skew Run 3 with smaller low-altitude shear is the two-dimensional vorticity structure at $z = 0.15$: Run 2 exhibits a dipole structure while Run 3 retains the cyclonic monopole structure seen in the benchmark Run 0. With VHTs occurring more closely in space and time, one might anticipate vortex merger among the cyclones of Run 3, but not among the dipoles of Run 2. Figures 18 and 19 confirm that expectation, and should be compared to figure 7. An effect of the shear in Run 3 is to limit the vertical extent of the emergent moist vortex to altitudes below $z = 0.45$, whereas the vortex structure of Run 0 does not deteriorate until altitudes near $z = 0.60$. The non-skew Run 1 is more like Run 0 with respect to skewness values
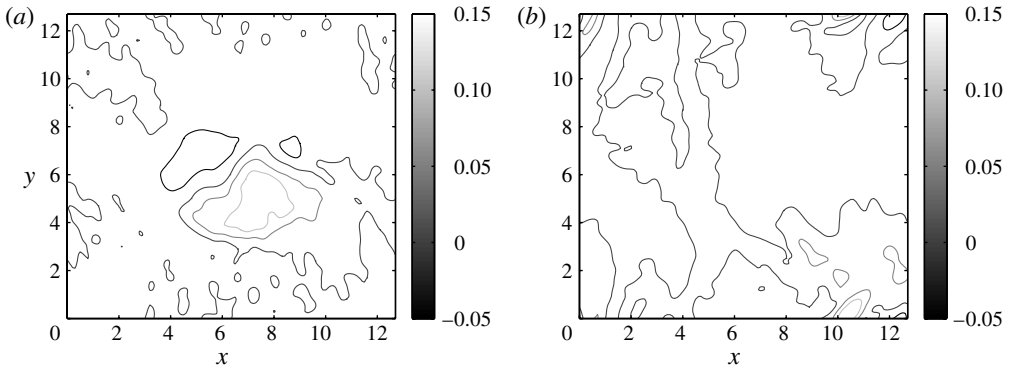
FIGURE 18. Two-dimensional vertical vorticity contours for bottom-skew Run 2 at altitudes (*a*) 1.5 km and (*b*) 3.0 km. The time is 9 h into the decay period. One unit of vorticity $= 10^{-3}$ s^{-1}.
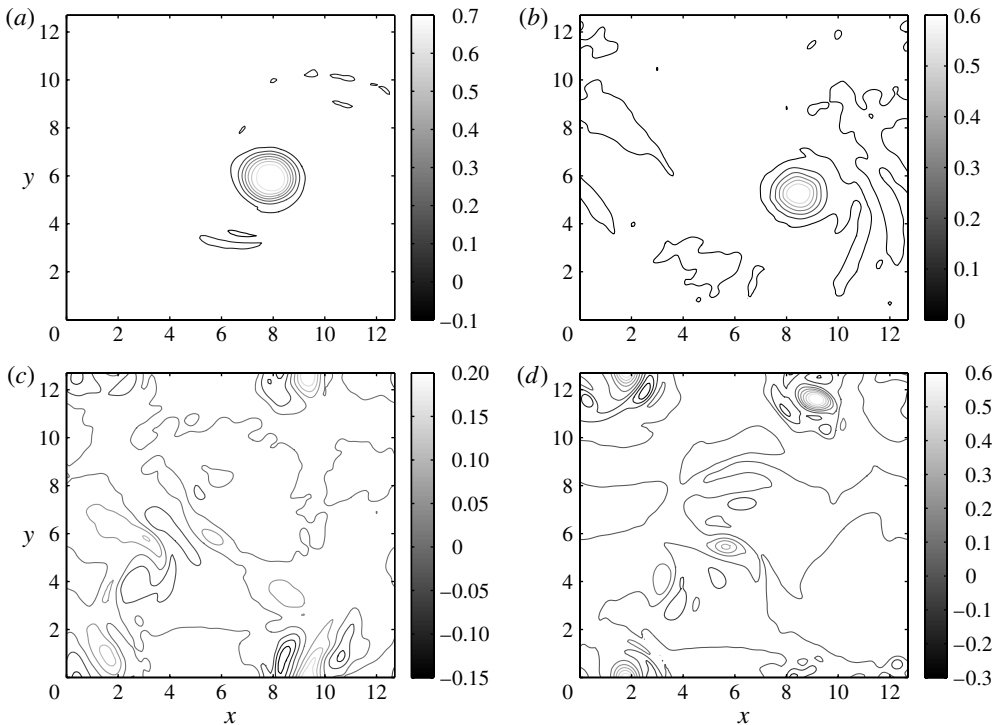

FIGURE 19. Two-dimensional vertical vorticity contours for top-skew Run 3 at altitudes (*a*) 1.5 km, (*b*) 3.0 km, (*c*) 4.5 km and (*d*) 6.0 km. The time is 9 h into the decay period. A larger-scale vortex extends up to 3.0 km. One unit of vorticity $= 10^{-3}$ s^{-1}.

(table 1), but 'intermediate' between Runs 0 and 2 with respect to individual VHT structure: the monopole structure is beginning to break down (figure 13). Furthermore, figure 20 shows that Run 1 behaves similarly to Run 2 for the decay period following convergence. No well-defined, vertically coherent vortex is formed in the presence
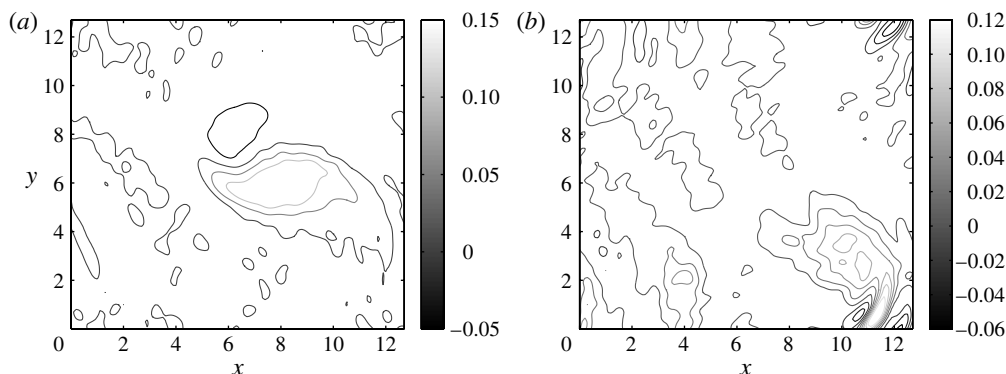
FIGURE 20. Two-dimensional vertical vorticity contours for non-skew Run 1 at altitudes (*a*) 1.5 km and (*b*) 3.0 km. The time is 9 h into the decay period. One unit of vorticity $= 10^{-3}$ s^{-1}.

of the stronger low-level shear values of Runs 1 and 2. Note that the time-averaged vertical vorticity skewness values at $z = 0.15$ remain positive for Run 1 ($S = 0.28$) and Run 2 ($S = 0.11$, see table 1), indicating a predominance of positive vertical vorticity even within the dipole structure, presumably because of the positive planetary vorticity. Hence for Run 2 with largest low-level vertical shear, there is still a tendency toward development of a larger-scale, low-altitude, amorphous structure with positive vertical vorticity (see figure 18 at $z = 0.15$).

4.3. *Sensitivity to the bottom boundary condition*

As mentioned in § 3, our set-up imagines that the lowest altitude is at the top of the atmospheric boundary layer. For simplicity, our first set of runs reported here used only zero Dirichlet or zero Neumann boundary conditions at top and bottom, and it may not be entirely clear which choice is more appropriate at the bottom of the domain. Therefore, in this section we compare the results of Runs 0 and 3 with zero Dirichlet bottom boundary conditions to Runs 4 and 5 with zero Neumann bottom boundary conditions (zero initial velocity Run 4 is the companion to zero initial velocity Run 0; top-skew Run 5 is the companion to top-skew Run 3). Our purpose here is to investigate whether or not the change in bottom boundary condition qualitatively alters the results found in Runs 0 and 3. The initial zonal velocity profile for Run 5 the same as for Run 3 and given by (4.3), which has near-zero slope at $z = 0$. Figure 21 shows the initial and later-time mean horizontal profiles for Runs 3 and 5. Non-zero velocity at $z = 0$ is evident for Run 5 at the later time, and clearly the lowest-level vertical shear has also been reduced (by necessity of the boundary condition).

For compactness, we present only two-dimensional contours of vertical vorticity, since we have seen above the robustness of the VHT structure for water vapour, vertical velocity and rain water. We first examine the low-altitude $z = 0.15$ vertical vorticity for representative VHTs during the 4-day period of low-frequency moisture forcing every 2.5 h, when the VHTs evolve independently from each other. Figure 22 compares Runs 0 and 4, both with zero initial velocity, and shows that the basic monopole structure does not depend on the bottom boundary condition. Similarly, figure 23 compares Runs 3 and 5 with top-skew initial velocity profiles, and again the
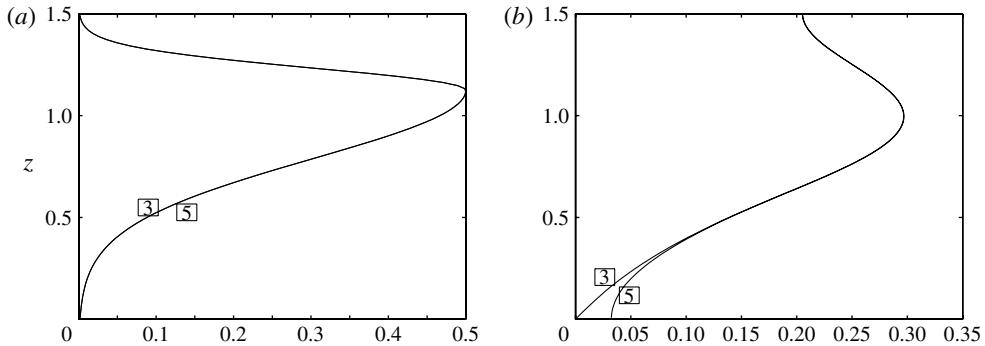
FIGURE 21. (*a*) Initial zonal velocity with $u(t = 0, z)$. (*b*) Horizontal mean velocity $\overline{U}(z) = (\bar{u}^2 + \bar{v}^2)^{1/2}(z)$ at $t = 400$ units (approximately 4 days). One velocity unit $= 10$ m s^{-1}; one height unit $= 10$ km. (a) $u(t = 0, z)$; (b) $(\bar{u}^2 + \bar{u}^2)^{1/2}$, $t = 400$.
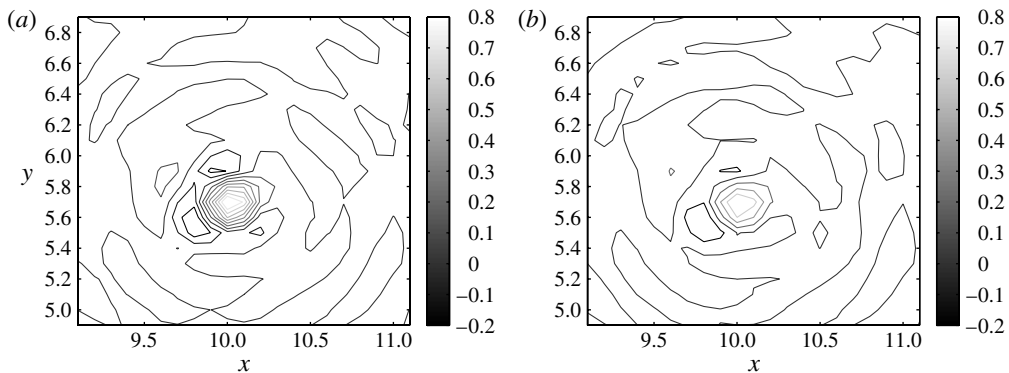

FIGURE 22. Two-dimensional vertical vorticity contours at $z = 1.5$ km for (*a*) Run 0 and (*b*) Run 4. Both runs have zero initial velocity and differ by the bottom boundary condition. Run 0 (Run 4) uses zero Dirichlet (Neumann) bottom boundary condition. The time is 30 min after a bubble injection. One vorticity unit $= 10^{-3}$ s^{-1}; one unit of distance $= 10$ km.

cyclonic monopole vorticity structure is evident. Notice also that the maximum and minimum contour values are the same in all Runs 0, 3, 4, 5.

Finally, we simulate the 2.6-day period of strong convergence, with moisture forcing every 7.5 min in the small horizontal domain 4 km $\times$ 4 km. We then allow the flow to decay and look for the formation of a larger-scale cyclone. During the convergence period, the VHTs interact nonlinearly with each other. Comparing figures 7 and 24 for the runs with zero initial velocity, one sees that the Neumann bottom boundary condition broadens the emergent moist vortex and reduces its amplitude. On the other hand, comparing figures 19 and 24 for the runs with top-skew initial velocity profiles, the Neumann bottom boundary condition leads to a larger-scale vortex which is relatively stronger at $z = 0.15$ and a weaker at $z = 0.30$. The latter result is consistent with the zero-shear boundary condition of Run 5. For both Runs 3 and 5, the low-altitude shear limits the vertical extent of the emergent vortex compared to Runs 0 and 4. Thus the shear appears to be more important than the bottom boundary
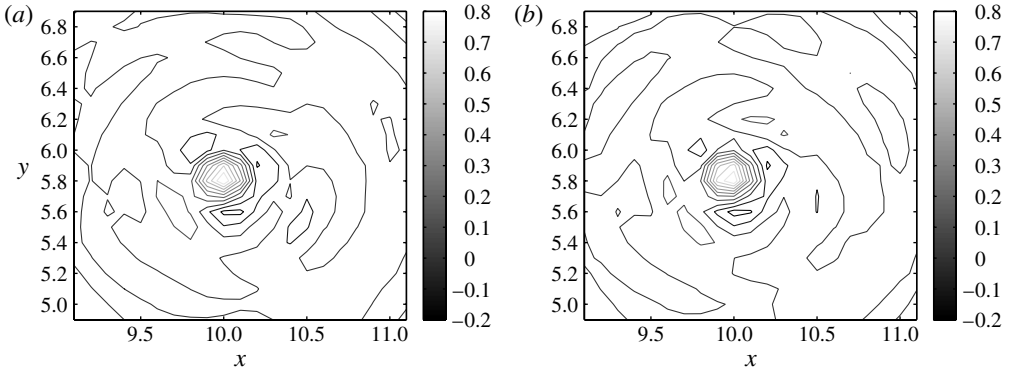
FIGURE 23. Two-dimensional vertical vorticity contours at $z = 1.5$ km for (*a*) Run 3 and (*b*) Run 5. Both runs have top-skew initial velocity and differ by the bottom boundary condition. Run 3 (Run 5) uses zero Dirichlet (Neumann) bottom boundary condition. The time is 30 min after a bubble injection. One vorticity unit $= 10^{-3}$ s^{-1}; one unit of distance $=$ 10 km.

condition in determining the vertical extent of the larger-scale vortex. However, the bottom boundary condition partly determines its horizontal extent and its amplitude.

4.4. *Increasing the latent heat factor*

It is important to investigate model sensitivity to various parameter values, and in particular to the non-dimensional latent heat factor $\epsilon^{-1}\mathscr{L}$ which was taken artificially low in our first study to allow for a larger time step. Here we demonstrate that similar results are obtained for the latent heat factor $\epsilon^{-1}\mathscr{L} \approx 8$ if other parameters are adjusted in a consistent manner. In order to compensate for the low latent heat $\epsilon^{-1}\mathscr{L} = 2.4$, Runs 0–5 used a large surface saturation value $\beta = 5$ in (2.6) corresponding to 50 g kg^{-1}. For the more realistic value $\epsilon^{-1}\mathscr{L} \approx 8$, we adjust $\beta = 5 \times (2/5) = 2$ in (2.6) corresponding to more realistic surface saturation level 20 g kg^{-1}. For consistency, the factor 2/5 is used to re-scale δ in (2.9), as well as the peak amplitude $(0.8 + \delta)$ of the water vapour bubble in (3.6). With these parameter changes and keeping the saturation profile only a function of altitude $q_{vs} = q_{vs}(z)$, the VHTs rise quickly and the moisture anomaly reaches the top of the simulation domain after approximately 20 min. Within the context of our simple model, there are two straightforward approaches to slowing the vertical propagation speed of the moisture anomaly: (i) increase the non-dimensional relaxation time scales α_d and α_r, which corresponds to increasing the time scales associated with condensation and evaporation in (2.5), or (ii) adopt a saturation profile q_{vs} that limits the altitude of the cloud tops. Here we present results using the the first approach.

Run 6 starts from zero initial velocity with realistic latent heat $\epsilon^{-1}\mathscr{L} \approx 8$, saturation level $\beta = 2$, and condensation/evaporation times scales $\alpha_d = \alpha_r = 0.45$. Figure 26 shows moisture anomaly contours at times 15 and 30 min after a bubble injection, and can be compared to figure 2 (the contour levels in figure 26 have been adjusted downward accordingly for the lower saturation levels). The cyclonic monopole structure of the VHT is clear from figure 27, though the maximum of vorticity $\approx 6 \times 10^{-4}$ s^{-1} at $z = 0.15$, $t = 30$ min is smaller than the maximum $\approx 8 \times 10^{-4}$ s^{-1} at $z = 0.15$, $t = 30$ min for Run 0 (see figures 3 and 4). Compared
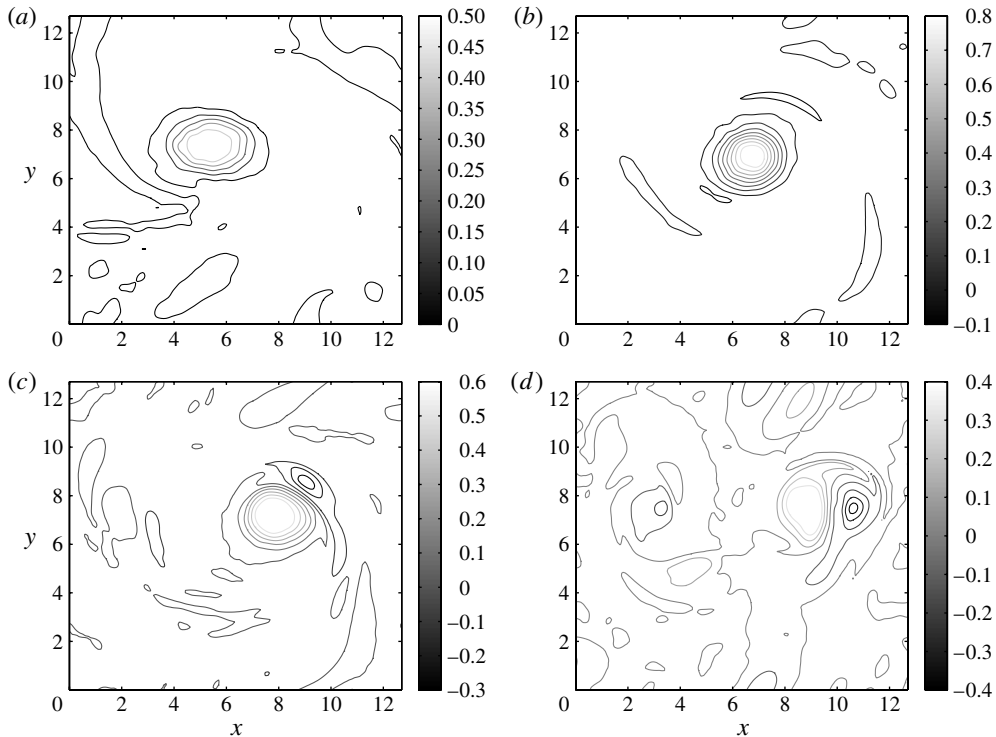
FIGURE 24. Two-dimensional vertical vorticity contours for Run 4 at altitudes (*a*) 1.5 km, (*b*) 3.0 km, (*c*) 4.5 km and (*d*) 6.0 km. Run 4 starts from zero initial velocity and uses zero Neumann bottom boundary condition. The time is 9 h into the decay period. One unit of vorticity $= 10^{-3}$ s^{-1}.

to Run 0, figures 28 and 29 show that the VHTs for Run 6 have higher cloud tops ($\approx$14 km high), lower precipitation (maximum $q_r \approx 7$ g kg^{-1}) and longer lifetimes ($\approx$1.5 h). Thus the basic features of the VHTs appear robust to changes in parameter values, though quantitative differences in structure are also apparent. In future quantitative studies, the parameters may be chosen to mimic reality as closely as possible.

5. Discussion and future work

The first goal of the work presented herein was to investigate the fidelity of moist Boussinesq dynamics with explicitly only two phases of water (vapour and rain), and using the simplest possible models for condensation and evaporation. Other complications found in atmospheric cloud resolving models such as turbulence models and sponge layers are also absent by design. Judging by the structure of individual VHTs generated by low-altitude moisture forcing, the simplified dynamics appears to capture the essential features of the VHTs. This result was anticipated by the multiscale analysis of MXM10. Differences in the moisture model, boundary conditions, background profiles and forcing render impossible a direct quantitative comparison of our runs and the simulations of WS11. Nevertheless, the qualitative comparison suggests that the minimal Boussinesq model is adequate for further
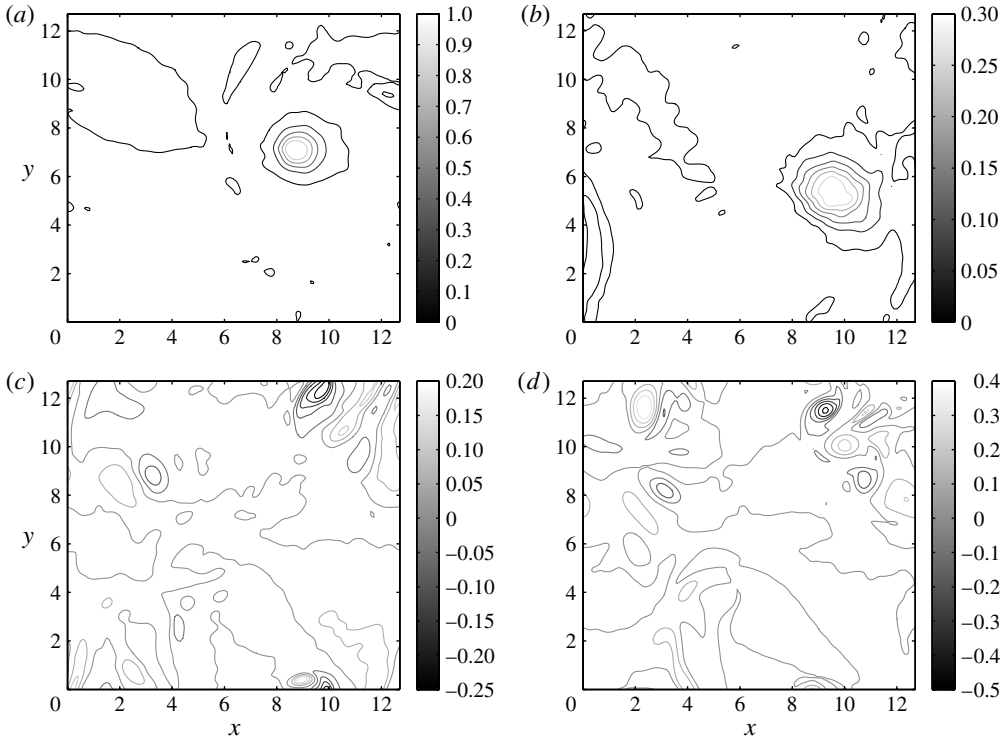
FIGURE 25. Two-dimensional vertical vorticity contours for top-skew Run 5 at altitudes (*a*) 1.5 km, (*b*) 3.0 km, (*c*) 4.5 km and (*d*) 6.0 km. Run 5 starts from a top-skew velocity and uses zero Neumann bottom boundary condition. The time is 9 h into the decay period. One unit of vorticity $= 10^{-3}\ \mathrm{s}^{-1}$.

investigation into the competing effects of moisture and shear, as well as other effects such as boundary conditions. One future project immediately accessible is a detailed study of the effects of inertia–gravity waves. The latter study will involve comparison of full Boussinesq simulations to simulations with WTG imposed, as well as comparison to computations of the MXM10 multiscale model in which WTG arises naturally as part of the dominant dynamics. It would also be interesting to perform a more quantitative comparison with a more complex cloud-resolving model.

The second goal was to begin a systematic study of the effects of low-altitude vertical shear on the structure and potential merger of VHTs. To study individual VHTs, we used a moisture forcing with frequency ~ 2.5 times larger than the lifetime of a single VHT (approximately 1 h). Increasing the low-level vertical shear changes the vertical vorticity structure from a cyclonic monopole to a dipole, as can be described by linear dynamics for short times in (4.7). Over long times (approximately 4 days), the vertical vorticity skewness (4.5) was used as a statistic to measure the predominance of cyclonic activity for runs with different vertical shear profiles. Somewhat surprisingly, the low-altitude skewness for Run 3 with small low-altitude vertical shear was larger than the skewness of Run 0 starting from zero initial velocity. To study the nonlinear interaction between VHTs as might occur during/after wind convergence in the atmospheric
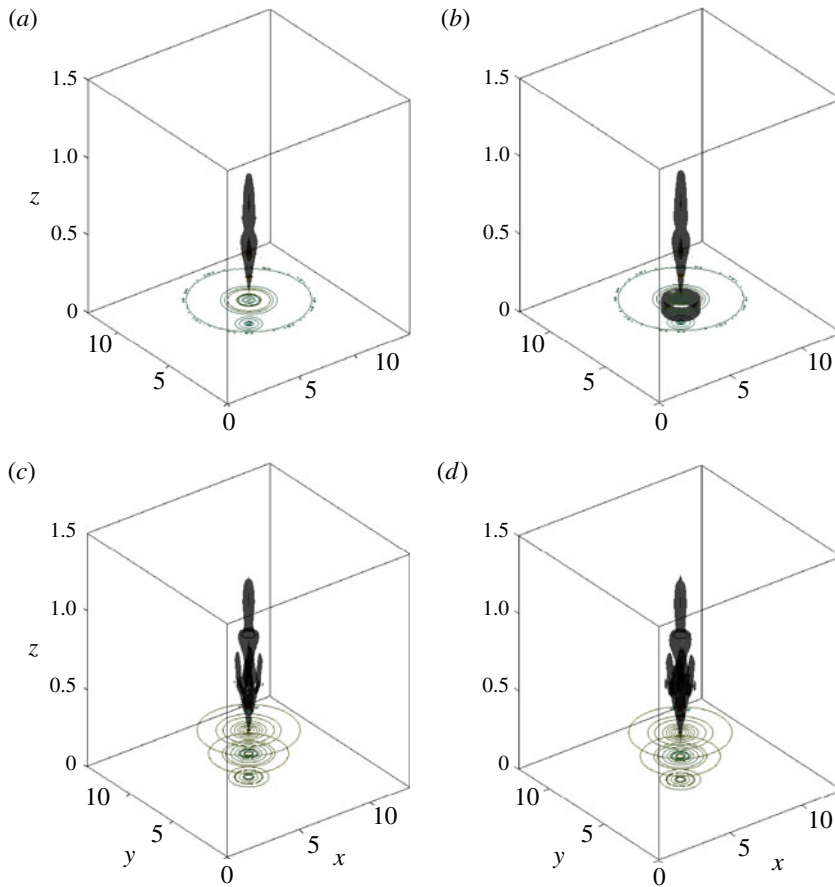
FIGURE 26. Moisture anomaly contours for Run 6 starting from zero initial velocity, with higher latent heat factor $\epsilon^{-1}\mathcal{L} \approx 8.0$, lower surface saturation value $\beta = 2$ and longer condensation/relaxation time scales $\alpha_d = \alpha_r = 0.45$. The times are (*a,b*) 30 min and (*c,d*) 45 min after the first bubble injection; the contour levels are (*a,c*) $(2/5) \times 1.2 = 0.48$ g kg^{-1} and (*b,d*) 0.30 g kg^{-1}. Compare with figure 2. One unit of distance $= 10$ km.

boundary layer, we increased the frequency of the moisture forcing to 7.5 min in a horizontal subdomain of 4 km $\times$ 4 km. After the forcing is turned off and for small shears (Runs 0, 3, 4, 5), the cyclonic monopoles merge together to generate a larger-scale cyclonic vortex. For sufficiently strong low-altitude vertical shear (Runs 1, 2), the individual VHTs show a tendency toward the dipole structure and 'convergence' does not yield a well-defined, vertically coherent, larger-scale vortex. We conclude that increasing low-altitude vertical shear has an adverse effect on the vertical vorticity structure of individual VHTs, which in turn affects the nonlinear interaction (possibility for merger) between VHTs. In low-shear cases when monopoles merge into a larger-scale vortex, vertical shear limits the height of the emergent vortex.

Our idealized simulations have initiated a study of mechanisms by which increasing vertical shear inhibits cyclogenesis. Future research will address issues such as shear thresholds, necessary size/strength of 'convergence zones', detailed analysis
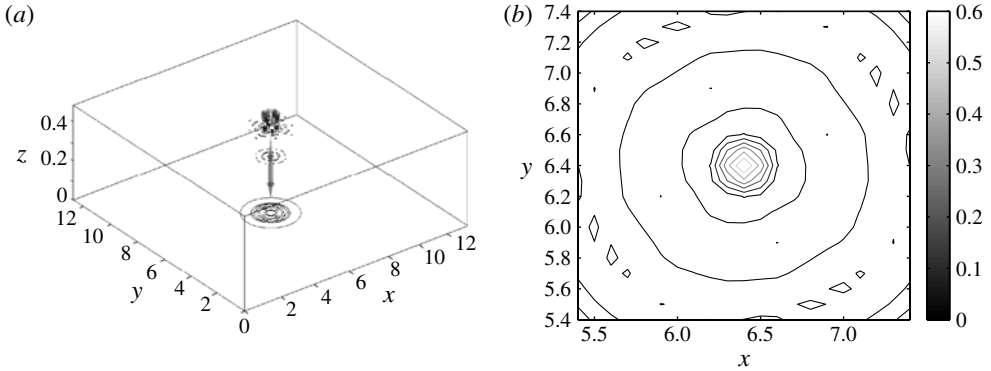
FIGURE 27. (*a*) Three-dimensional vertical vorticity contours for Run 6 (light grey = 3×10^{-4} s^{-1}, dark grey = -3×10^{-4} s^{-1}). (*b*) Two-dimensional vertical vorticity contours at altitude $z = 1.5$ km. The time is 30 min after a bubble injection. Compare with figures 3 and 4. One vorticity unit = 10^{-3} s^{-1}; one unit of distance = 10 km.
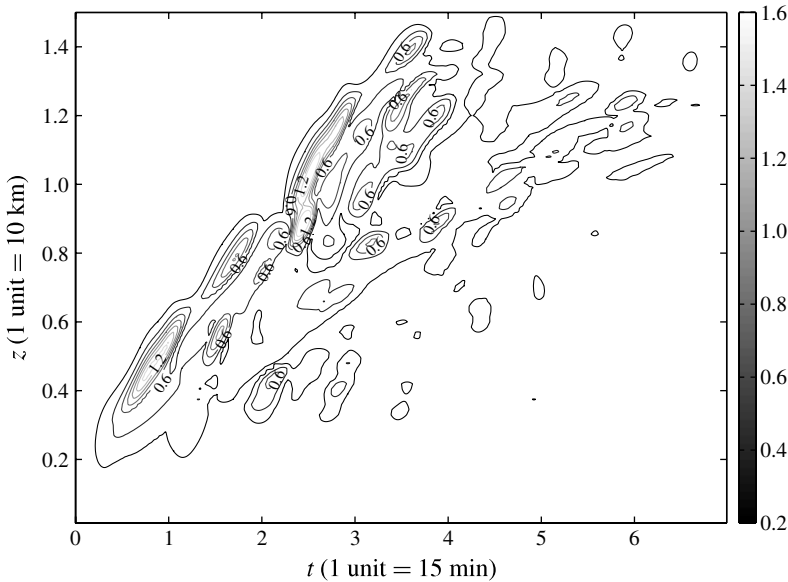

FIGURE 28. Maximum vertical velocity versus time (abscissa) and altitude (ordinate) for Run 6: lifetime ≈1.5 h; one velocity unit = 10 m s^{-1}. Contours are spaced by 0.2 velocity units.

of momentum transport terms, and the role of a background preconditioning weak depression with vertical structure (Montgomery *et al.* 2006; Majda *et al.* 2008).

Acknowledgements

The authors would like to thank S. Stechmann and J. Sukhatme for many fruitful discussions, as well as M. Montgomery, R. Klein and F. Waleffe for helpful comments on an earlier draft of the manuscript. Q.D. and L.M.S. are grateful for the support
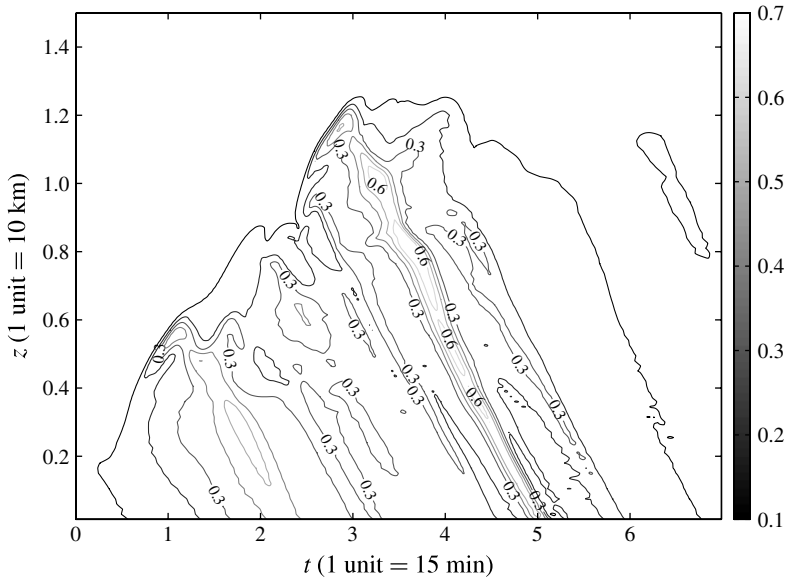
FIGURE 29. Maximum liquid water versus time (abscissa) and altitude (ordinate) for Run 6: lifetime ≈ 1.5 h; one unit of rain water $= 10$ g kg^{-1}. Contours are spaced by 0.2 units of rain water.

REFERENCES

BRYAN, G. H. & FRITSCH, J. M. 2002 A benchmark simulation for moist nonhydrostatic numerical models. *Mon. Wea. Rev.* **130**, 2917–2928.

CHARNEY, J. G. & ELIASSEN, A. 1964 On the growth of the hurricane depression. *J. Atmos. Sci.* **21**, 68–75.

CURRY, J. A. & WEBSTER, P. J. 1999 *Thermodynamics of Atmospheres and Oceans*. Academic.

DAVIS, C. A. & BOSART, L. F. 2004 The TT problem: forecasting the tropical transition of cyclones. *Bull. Am. Meteorol. Soc.* **85**, 1657–1662.

EMANUEL, K. A. 1986 An air–sea interaction theory for tropical cyclones. Part 1. Steady state maintenance. *J. Atmos. Sci.* **43**, 585–604.

EMANUEL, K. A. 1989 The finite-amplitude nature of tropical cyclogenesis. *J. Atmos. Sci.* **46**, 3431–3456.

EMANUEL, K. A. 2003 Tropical cyclones. *Annu. Rev. Earth Planet. Sci.* **31**, 75–104.

FRIERSON, D. M. W., PAULUIS, O. & MAJDA, A. J. 2004 Large scale dynamics of precipitation fronts in the tropical atmosphere: a novel relaxation limit. *Commun. Math. Sci.* **2**, 591–626.

GRABOWSKI, W. W. & SMOLARKIEWICZ, P. K. 1996 Two-time-level semi-Lagrangian modelling of precipitating clouds. *Mon. Wea. Rev.* **124**, 487–497.

GRABOWSKI, W. W. & CLARK, T. L. 1991 Cloud-environment interface instability: rising thermal calculations in two spatial dimensions. *J. Atmos. Sci.* **48**, 527–546.

GRABOWSKI, W. W. & CLARK, T. L. 1993a Cloud-environment interface instability. Part 2. Extension to three spatial dimensions. *J. Atmos. Sci.* **50**, 555–573.

GRABOWSKI, W. W. & CLARK, T. L. 1993b Cloud-environment interface instability. Part 3. Direct influence of environmental shear. *J. Atmos. Sci.* **50**, 3821–3828.

GRAY, W. M. 1968 Global view of the origin of tropical disturbances and storms. *Mon. Wea. Rev.* **96**, 669–700.

HENDRICKS, E. A., MONTGOMERY, M. T. & DAVIS, C. A. 2004 The role of vortical hot towers in the formation of tropical cyclone Diana (1984). *J. Atmos. Sci.* **61**, 1209–1232.

HENDRICKS, E. A. & MONTGOMERY, M. T. 2006 Rapid scan views of convectively generated mesovortices in sheared tropical cyclone Gustav (2002). *Weather Forecast.* **21**, 1041–1050.

HOUZE, R. A. JR., LEE, W.-C. & BELL, M. M. 2009 Convective contribution to the genesis of hurricane Ophelia (2005). *Mon. Wea. Rev.* **137**, 2778–2800.

KLEIN, R. & MAJDA, A. J. 2006 Systematic multiscale models for deep convection on mesoscales. *Theor. Comput. Fluid Dyn.* **20**, 525–551.

MAJDA, A. 2002 *Introduction to PDEs and Waves for the Atmosphere and Ocean*. Courant Institute of Mathematical Sciences.

MAJDA, A.J. 2007 Multiscale models with moisture and systematic strategies for superparameterization. *J. Atmos. Sci.* **64**, 2726–2734.

MAJDA, A. J., XING, Y. & MOHAMMADIAN, M. 2008 Vertically sheared horizontal flow with mass sources: a canonical balanced model. *Geophys. Astrophys. Fluid. Dyn.* **102**, 543–591.

MAJDA, A.J. & XING, Y. 2010 New multi-scale models on mesoscales and squall lines. *Comm. Math. Sci.* **8**, 113–134.

MAJDA, A. J., XING, Y. & MOHAMMADIAN, M. 2010 Moist multi-scale models for the hurricane embryo. *J. Fluid Mech.* **657**, 478–601.

MOLINARI, J., VOLLARO, D. & CORBOSIERO, K. L. 2004 Tropical cyclone formation in a sheared environment: a case study. *J. Atmos. Sci.* **61**, 2493–2509.

MONTGOMERY, M. T., NICHOLLS, M. E., CRAM, T. A. & SAUNDERS, A. B. 2006 A vortical hot tower route to tropical cyclogenesis. *J. Atmos. Sci.* **63**, 355–386.

MONTGOMERY, M. T. & SMITH, R. K. 2011 Paradigms for tropical-cyclone intensification. *Q. J. R. Meteorol. Soc.* **137**, 1–31.

OOYAMA, K. 1964 A dynamical model for the study of tropical cyclone development. *Geophys. Int.* **4**, 187–198.

OOYAMA, K. 1969 Numerical simulation of the life cycle of tropical cyclones. *J. Atmos. Sci.* **26**, 3–40.

OOYAMA, K. 1982 Conceptual evolution of the theory and modelling of the tropical cyclone. *J. Meteor. Soc. Japan* **60**, 369–379.

REMMEL, M. & SMITH, L. M. 2009 New intermediate models for rotating shallow water and an investigation of the preference for anticyclones. *J. Fluid Mech.* **635**, 321–359.

RIEHL, H. & MALKUS, J. S. 1958 On the heat balance of the equatorial trough zone. *Geophysica* **6**, 503–538.

RIEMER, M., MONTGOMERY, M. T. & NICHOLLS, M. E. 2010 A new paradigm for intensity modification of tropical cyclones: thermodynamic impact of vertical wind shear on the inflow layer. *Atmos. Chem. Phys.* **10**, 3163–3188.

ROTUNNO, R. & EMANUEL, K. 1987 An air–sea interaction theory for tropical cyclones. Part 2. Evolutionary study using a nonhydrostatic axisymmetric numerical model. *J. Atmos. Sci.* **44**, 542–561.

SIMPSON, J., HALVERSON, J. B., FERRIER, B. S., PETERSEN, W. A., SIMPSON, R. H., BLAKESLEE, R. & DURDEN, S. L. 1998 On the role of hot towers in tropical cyclone formation. *Meteorol. Atmos. Phys.* **67**, 15–35.

SMITH, L. M. & LEE, Y. 2005 On near resonances and symmetry breaking in forced rotating flows at moderate Rossby number. *J. Fluid Mech.* **535**, 111–142.

SPYKSMA, K., BARTELLO, P. & YAU, M. K. 2006 A Boussinesq moist turbulence model. *J. Turbul.* **7**, 1–24.

SUKHATME, J., MAJDA, A. J. & SMITH, L. M. 2012 Two-dimensional moist stratified turbulence and the emergence of vertically sheared horizontal flows. *Phys. Fluids* **24**, 036602.

SUKHATME, J. & SMITH, L. M. 2007 Self-similarity in decaying two-dimensional stably stratified adjustment. *Phys. Fluids* **19**, 036603.

WISSMEIER, U. & SMITH, R. K. 2011 Tropical-cyclone intensification: the effects of ambient vertical vorticity. *Q. J. R. Meteorol. Soc.* **137**, 854–857.